

TRANSPARENT ALUMINA CERAMICS FABRICATED USING 3D  
PRINTING AND VACUUM SINTERING

BY

DAVID M. CARLONI

A THESIS  
SUBMITTED TO THE FACULTY OF

ALFRED UNIVERSITY

IN PARTIAL FULFILLMENT OF THE REQUIREMENTS  
FOR THE DEGREE OF

MASTER OF SCIENCE

IN

MATERIALS SCIENCE AND ENGINEERING

ALFRED, NEW YORK

APRIL, 2020

TRANSPARENT ALUMINA CERAMICS FABRICATED USING 3D  
PRINTING AND VACUUM SINTERING

BY

DAVID M. CARLONI

B.S. ALFRED UNIVERSITY (2018)

SIGNATURE OF AUTHOR \_\_\_\_\_

APPROVED BY \_\_\_\_\_

YIQUAN WU, ADVISOR

\_\_\_\_\_  
STEVEN TIDROW, ADVISORY COMMITTEE

\_\_\_\_\_  
ANTHONY WREN, ADVISORY COMMITTEE

\_\_\_\_\_  
WILLIAM CARLSON, CHAIR, ORAL THESIS DEFENSE

ACCEPTED BY \_\_\_\_\_

GABRIELLE GAUSTAD, DEAN  
KAZUO INAMORI SCHOOL OF ENGINEERING

Alfred University theses are copyright protected and may be used for education or personal research only. Reproduction or distribution in part or whole is prohibited without written permission from the author.

Signature page may be viewed at Scholes Library, New York State College of Ceramics, Alfred University, Alfred, New York.

## **ACKNOWLEDGMENTS**

I would like to acknowledge my parents and my brother Joe for their support in my academic career. Furthermore, I would like to acknowledge my advisor, Dr. Yiquan Wu for the opportunity to perform this research investigation and for his guidance throughout, as well as my other colleagues in our research group for their help, including Elo Chen, Xuan Chen, Fang Guan, Yiyu Li, Ting Liu, Iva Milisavljevic, Shengquan Yu, and Guangran Zhang. Finally, I would like to acknowledge the faculty and staff who helped in this work, including my advisory committee of Dr. Steven Tidrow and Dr. Anthony Wren as well as Dr. Darren Stohr and Francis Williams. I am very thankful for everyone and their contributions.

# TABLE OF CONTENTS

	<b>Page</b>
Acknowledgments .....	iii
List of Tables .....	vi
List of Figures .....	vii
Abstract.....	ix
<b>I. INTRODUCTION .....</b>	<b>1</b>
A. TRANSPARENT CERAMICS.....	1
1. Background .....	1
2. Materials for Transparent Ceramics .....	3
3. Material Preparation and Synthesis Methods .....	7
4. Transparent Ceramic Processing Methods .....	8
B. 3D PRINTING OF CERAMICS .....	14
1. Background .....	14
2. Methods and Technologies.....	15
3. Current State and Future of Ceramic 3D Printing .....	25
C. AIMS OF THIS WORK.....	27
<b>II. STARTING MATERIALS AND SLURRY PREPARATION .....</b>	<b>28</b>
A. INTRODUCTION .....	28
B. EXPERIMENTAL PROCEDURE .....	29
C. RESULTS AND DISCUSSION .....	31
D. CONCLUSIONS.....	36
<b>III. 3D PRINTING AND CIP PROCESSING .....</b>	<b>37</b>
A. INTRODUCTION .....	37
B. EXPERIMENTAL PROCEDURE .....	39
1. 3D Printing .....	39
2. CIP Processing .....	40
C. RESULTS AND DISCUSSION .....	41
1. 3D Printed Samples .....	41
2. CIP Samples .....	47
D. CONCLUSIONS.....	48
<b>IV. POST-PROCESSING.....</b>	<b>48</b>
A. INTRODUCTION .....	48
B. EXPERIMENTAL PROCEDURE .....	49

C.	RESULTS AND DISCUSSION .....	50
D.	CONCLUSIONS.....	60
<b>V.</b>	<b>SUMMARY AND CONCLUSIONS .....</b>	<b>60</b>
<b>VI.</b>	<b>FUTURE WORK.....</b>	<b>61</b>
<b>VII.</b>	<b>REFERENCES.....</b>	<b>62</b>
<b>VIII.</b>	<b>APPENDIX.....</b>	<b>80</b>
1.	Table of Relative Density and Grain Size Data Among Sintered Samples. ....	80

## LIST OF TABLES

	<b>Page</b>
Table 1. Overview of Commonly Used Transparent Ceramic Materials. ....	6
Table 2. Overview of Popular AM Technologies.....	24

# LIST OF FIGURES

	<b>Page</b>
Figure 1. Scattering sources in polycrystalline ceramics, adapted from Ikesue et al. <sup>12</sup> .....	2
Figure 2. Schematic of a dry-press process. ....	10
Figure 3. Schematic of a CIP process. ....	10
Figure 4. Schematics of popular AM techniques, adapted from Zocca, Colombo, Gomes, and Günster . <sup>96</sup> .....	16
Figure 5. XRD analysis of prepared Al <sub>2</sub> O <sub>3</sub> powder.....	32
Figure 6. Particle size and distribution of prepared Al <sub>2</sub> O <sub>3</sub> powder.....	32
Figure 7. SEM image of prepared Al <sub>2</sub> O <sub>3</sub> powder. ....	33
Figure 8. Rheology of slurries with varying alumina content. ....	35
Figure 9. Rheology of slurries with varying isobam per mixed powder. ....	35
Figure 10. Diagram of Hyrel System 30M 3D printer.....	38
Figure 11. 3D printed alumina ceramics.....	41
Figure 12. Printing time as a function of print move speed.....	42
Figure 13. Printing time as a function of nozzle size.....	43
Figure 14. Printing time as a function of layer height. ....	45
Figure 15. Green density as a function of layer height.....	45
Figure 16. Alumina ceramics 3D printed with varying extrusion widths.....	46
Figure 17. CIP processed alumina ceramic.....	47
Figure 18. 3D printed transparent alumina ceramics. ....	51

Figure 19. Progression of a representative sample through the process. ....	51
Figure 20. XRD analysis of sintered alumina ceramics.....	52
Figure 21. Relative density as a function of sintering temperature for 6-hour hold time.....	53
Figure 22. Relative density as a function of sintering time at 1850°C. ....	54
Figure 23. Relative sintered density at 1850°C for 6 hours as a function of layer height.....	54
Figure 24. Average grain size as a function of SSS time at 1850°C. ....	55
Figure 25. SEM microstructure images of SSS ceramics at 1850°C for varying times. .	56
Figure 26. Average grain size as a function of sintering temperature for SSS and TSS ceramics. ....	56
Figure 27. SEM microstructure images of SSS ceramics sintered at varying temperatures for 6 hours. ....	57
Figure 28. SEM microstructure images of TSS ceramics sintered at varying temperatures.....	57
Figure 29. Total transmittance measurements for alumina ceramics from 3D printing and CIP.....	59

## **ABSTRACT**

Transparent alumina ceramics were fabricated using an extrusion-based 3D printer and post-processing steps, including debinding, vacuum sintering, and polishing. Printable slurry recipes and 3D printing parameters were optimized to fabricate quality green bodies of varying shapes and sizes. Post-process two-step vacuum sintering was found to increase density while reducing grain size and thus improving the transparency of the sintered alumina ceramics in comparison to single-step sintering. The 3D printed and two-step vacuum sintered alumina ceramics achieved greater than 99% relative density and total transmittance values of approximately 61% at 400 nm and 70% at 800 nm and above, which was comparable to that of conventional CIP processed alumina ceramics. This demonstrates the capability of 3D printing to compete with conventional transparent ceramic forming methods along with the additional benefits of freedom of design, production of complex shapes, and others.

# I. INTRODUCTION

## A. Transparent Ceramics

### 1. Background

Transparent polycrystalline ceramics have received significant attention and development around the world in recent years for optical applications over more conventional single crystal and glass materials. The technology behind transparent polycrystalline ceramics can be considered to have been invented by Robert L. Coble and General Electric (GE) in the early 1960's with their patent of "Transparent alumina and method of preparation"<sup>1</sup> and sale of the Lucalox™ sodium vapor lamp. This lamp was a result of research conducted at GE on sintering of Al<sub>2</sub>O<sub>3</sub> (alumina) ceramics that yielded a pore-free polycrystalline material which, at the time, exhibited novel transmittance and corrosion resistance properties and was significantly more cost-effective to produce than single crystal alumina (sapphire). Lucalox has been considered to be a revolution in lighting technology and led to further research and development in the area of transparent polycrystalline ceramics.<sup>2-3</sup>

In the many years that have followed, significant progress has continued to be made in developing transparent polycrystalline ceramics. Currently, transparent polycrystalline ceramics have been well-demonstrated in areas such as the aerospace and defense industries for windows and domes,<sup>4-5</sup> laser materials,<sup>6-7</sup> armor<sup>4, 8</sup> and other applications which require high performance even under potentially extreme environments.<sup>9</sup> Along with their wide range of relatively inexpensive and efficient processing options, transparent polycrystalline ceramics have shown the ability to achieve thermal, mechanical, and optical properties which are comparable to or even surpass that of transparent single crystals and glasses.<sup>4-5, 7-8, 10-12</sup> Single crystal fabrication, despite typically yielding excellent properties, requires long and expensive growth and machining processes to obtain a usable product. This somewhat limits the production of single crystal materials unless they are absolutely needed for the application. On the other hand, glasses typically do not exhibit the robust mechanical and thermal properties of ceramics. Hence, polycrystalline ceramics are well-

balanced and versatile materials that combine both desirable properties and processing options.<sup>9</sup>

Polycrystalline ceramic materials still pose many processing challenges towards achieving transparency, though, due to their inherent scattering sources that are not typically exhibited by single crystals and glasses. These scattering sources include grain boundaries, pores, secondary phases and impurities, and surface roughness. Furthermore, materials which possess asymmetric crystal structures present additional birefringence or double-refraction effects (optical anisotropy). These scattering sources are represented schematically in **Figure 1** which was adapted from Ikesue et al.<sup>13</sup> All of these combined attributes limit the amount of light which can be transmitted through the material. Through modern technology, careful design, and proper processing, however, it has been possible to reduce the effect of, or even remove, the scattering sources in polycrystalline materials, making them transparent.<sup>9, 12, 14-15</sup> The passing years have brought and continue to bring additional research and technological developments that provide improvements and new opportunities and within this field. The below section provides information on the current state of transparent polycrystalline ceramics in terms of materials and processing.

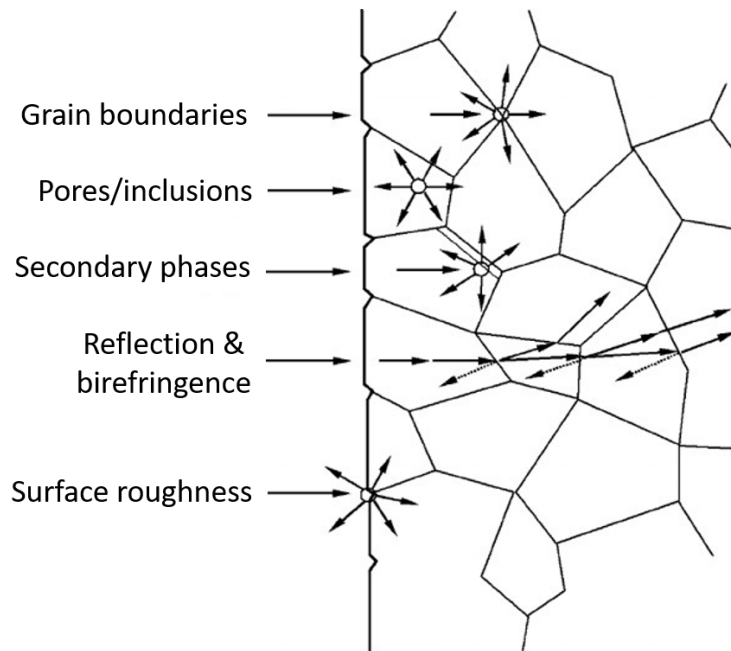


Figure 1. Scattering sources in polycrystalline ceramics, adapted from Ikesue et al.<sup>12</sup>

## 2. Materials for Transparent Ceramics

Proper starting materials are necessary to make transparent ceramics and there are currently a variety to choose from. To maximize optical quality, it is typically preferred that the material possess an optically isotropic crystal structure so as to eliminate the birefringence (double-refraction) effect which can be experienced across the grain boundaries of optically anisotropic materials. Additionally, dopants and additives are often included in small quantities to achieve more desirable properties or for specific applications. This section will provide information on commonly used materials for the fabrication of transparent polycrystalline ceramics as well as summarize some of the research that has been performed and applications for these materials. **Table 1** is presented at the end of this section and displays a summary of the materials covered along with some of their typical properties and the reports and references used throughout this paper.

Aluminum oxide ( $\alpha$ -Al<sub>2</sub>O<sub>3</sub>), also referred to as alumina, is a well-known and versatile ceramic which is notable for its high strength and hardness as well as being the first polycrystalline transparent ceramic material as invented by Coble and GE.<sup>1-2, 16-21</sup> Alumina possesses an optically anisotropic crystal structure which somewhat limits its optical properties in comparison to other materials. Therefore fast consolidation processes and sintering aids, like MgO, are typically used to reduce the grain size in relation to the wavelength of light, thus mitigating the birefringence effect.<sup>22</sup> Alternatively, oriented grains can be achieved through the application of a strong magnetic field during processing.<sup>23</sup> Despite these processing hurdles, transparent alumina ceramics have still been widely reported for a variety of fabrication methods and applications, most notably for use as transparent armor and protective windows in extreme environments due to the rugged properties.<sup>8, 24</sup> Peelen et al. studied transparent alumina extensively and produced two comprehensive papers on the light scattering and optical properties of alumina.<sup>14, 17</sup> Krell et al. reported on using sintering and hot isostatic pressing (HIP) to achieve near full density and submicron grain size transparent alumina ceramics with 55-65% in-line transmission as well as high microhardness and bending strength.<sup>25</sup> In a different study Grasso et al. used high-pressure spark plasma sintering (SPS) to fabricate pure alumina ceramics which achieved 65.4% transmission and less than 200 nm grain sizes.<sup>26</sup> Mata-

Osoro and coworkers demonstrated slip cast processed transparent alumina ceramics prepared using vacuum sintering as well as conventional sintering in air.<sup>27</sup>

Similar to alumina, aluminum oxynitride (AlON) also exhibits great mechanical properties, but possesses the optically isotropic cubic spinel crystal structure which enables it to typically achieve improved transmission properties. ALON™ is the marketed name for AlON as patented by Raytheon Company in 1985 and currently assigned to Surmet Corporation.<sup>28</sup> AlON is primarily manufactured using proprietary processing methods for applications such as transparent armor as well as domes and windows for missiles and aircraft. AlON sometimes incorporates an additional non-reflective coating to achieve improved transmission.<sup>29-31</sup> Jiang et al. reported on transparent AlON ceramic pellets fabricated using cold isostatic pressing (CIP) followed by pressureless sintering and hot isostatic pressing (HIP) post-treatment which achieved transmittance values as high as 84.8% at 600 nm (visible range) and 86.1% at 2000 nm (near-infrared range).<sup>32</sup> Kumar and Johnson have also reported transparent AlON ceramics fabricated using slip casting and vacuum sintering with in-line transmittance values of approximately 80% in the wavelength region from 0.22 – 6 μm.<sup>33</sup> A study on properties including, but not limited to, optical scatter, refractive index, and absorption of AlON transparent ceramics of varying composition was conducted by Hartnett et al. as well.<sup>34</sup>

Magnesium aluminate spinel ( $MgAl_2O_4$ ), often referred to as just “spinel”, is a well-rounded material with good optical, mechanical, and thermal properties which also possesses the cubic spinel crystal structure. Unlike AlON, magnesium aluminate spinel powders and processing methods are not proprietary, enabling relatively inexpensive and easier routes to utilize this material.<sup>35</sup> Transparent polycrystalline spinel ceramics have also been primarily of interest in applications such as transparent armor and protective windows for sensors and high energy lasers in harsh environments.<sup>8, 36</sup> Tokariev and coworkers conducted a study on the mechanical properties and grain size effects of transparent polycrystalline spinel ceramics fabricated via uniaxial pressing followed by vacuum sintering and post HIP treatment.<sup>37</sup> Khasanov et al. reported on transparent polycrystalline spinel ceramics formed under varying SPS parameters which achieved 72.6% transmission at a wavelength of 555 nm as well as a high microhardness of 18.52 GPa and Young’s modulus of 212 GPa.<sup>38</sup>

Yttrium Oxide ( $Y_2O_3$ ), also known as yttria, was originally invented in 1966 by GE and Richard C. Anderson as a  $ThO_2$ -doped yttria product under the trade name Yttralox™ which was later patented in 1970.<sup>39</sup> Yttria possesses the cubic bixbyite crystal structure and exhibits excellent optical and thermal properties as well as a wide transmission range, but is relatively lacking in mechanical properties. The mechanical properties somewhat limited yttria to applications in environments which are less extreme and do not require a high level of durability. Efforts have been made, however, to achieve more desirable mechanical properties (as well as optical and thermal properties) through doping, enabling yttria to be used in applications such as IR windows and domes for missiles as well as solid-state lasers. Hogan et al. conducted a fairly comprehensive review and study on transparent polycrystalline yttria ceramics including a comparison of studies on undoped and  $La_2O_3$ -doped yttria showing significantly improved optical, thermal, and mechanical properties with doping due to controlled grain growth.<sup>40-41</sup> Hou et al. reported on and investigated the mechanisms behind the use of another dopant, zirconia ( $ZrO_2$ ), to fabricate isostatically pressed yttria disks which were sintered under vacuum and achieved transmittance values as high as 83.1% when the zirconia content was optimized.<sup>42</sup> Yttria was also one of the first polycrystalline materials to be reported for application in solid-state lasers by Greskovich and Chernoch in 1973 with their study on Nd-doped Yttralox.<sup>43</sup> In a more recent study, Kong et al. reported on a high power 9.2 W diode-end-pumped polycrystalline Yb-doped yttria ceramic ( $Yb:Y_2O_3$ ) which demonstrated higher laser efficiency than single crystal yttrium aluminum garnet (YAG) with the same dopant.<sup>44</sup>

Yttria Alumina Garnet ( $Y_3Al_5O_{12}$ ), commonly abbreviated as YAG, combines the useful properties of both yttria and alumina and is highly studied in the field of transparent ceramics for solid-state laser applications. YAG is commonly used in conjunction with dopants of rare-earth ions because they can easily substitute for the yttrium ions of the host lattice due to their similar size and same valence state (+3) as well as their useful range of emission wavelengths.<sup>45</sup> Although YAG is more conventionally used as a single crystal, Ikesue and coworkers have conducted multiple studies on polycrystalline Nd:YAG and have demonstrated that the polycrystalline ceramics can exhibit optical and laser properties that match, or even surpass, that of single crystal Nd:YAG ceramics grown by the Czochralski method.<sup>46-48</sup> In more recent studies, Zhou et al. fabricated highly transparent

polycrystalline YAG ceramics with varying levels of MgO dopant via isostatic pressing and subsequent vacuum sintering which achieved transmittance values as high as 84.5% at a wavelength of 1064 nm.<sup>49</sup> Wagner et al. also conducted a study on transparent Ce:YAG ceramic phosphors fabricated via SPS and post-sintering HIP treatment which achieved about 82% in-line transmission at a wavelength of 530 nm and exhibited sufficient photoluminescence intensity, making it a good candidate for high-powered light emitting diode (LED) applications.<sup>50</sup>

Table 1. Overview of Commonly Used Transparent Ceramic Materials.

Material	Density (g/cm <sup>3</sup> )	Transmission Range (μm)	Melting Point (°C)	Young's Modulus (GPa)	Knoop Hardness (kg/mm <sup>2</sup> )	Typical Applications	References & Reports
<b>Al<sub>2</sub>O<sub>3</sub></b>	3.98	0.2-6.0	2072	345-400	1500-2200	Armor, windows/domes	1-3, 8, 9, 13, 15-25, 71
<b>AlON</b>	3.70	0.2-6.0	2150	321-323	1850-1950	Armor, windows/domes	4, 5, 8, 9, 26-32
<b>MgAl<sub>2</sub>O<sub>4</sub></b>	3.58	0.3-6.5	2135	270-277	1400-1650	Armor, windows/domes, lasers	4, 8, 9, 33-36, 56, 73, 79, 85, 183
<b>Y<sub>2</sub>O<sub>3</sub></b>	5.01	0.2-8.5	2157	165-174	650-720	Windows/domes, lasers, scintillators	7, 9, 37-42, 55, 57, 80, 84,
<b>YAG</b>	4.55	0.2-5.5	1940	200-300	1215	Lasers, scintillators	6, 7, 9, 20, 43-48, 54, 60, 68, 69, 72, 78, 81, 86, 87

### 3. Material Preparation and Synthesis Methods

In addition to the type of the material chosen, the process of preparing synthetic materials is another important consideration in transparent polycrystalline ceramic fabrication. Impurities and inhomogeneities can cause undesirable scattering, thus reducing the final optical quality which can be achieved by the ceramic. For good optical quality, raw powder materials of at least 99% purity are required and it is important to work in a clean environment. Additionally, the quality, homogeneity, and sintering of the final material is typically a function of the method used to prepare or synthesize the powder. Some of the most commonly used methods along with examples of their use in literature are discussed next.

Solid-state reaction (SSR) is probably the most widely used synthesis method. In SSR, powders are mixed in stoichiometric ratios for the desired final product, formed, and then heated to high temperatures. The powders react at the high temperatures to form a solid phase prior to densification.<sup>51</sup> This method is relatively simple and enables the use of commercial powder products, but it is necessary to understand the reaction kinetics and select the proper heating profile to ensure that the reaction achieves the desired composition and phase structure. Typically, powders are milled prior to SSR to achieve a homogeneous mixture as well as a finer particle size and higher surface area which maximizes the number of contact points and area of contact between particles. There have been many demonstrations of SSR in the fabrication of transparent ceramics, such as the works of Ikesue et al.,<sup>52</sup> Lee et al.,<sup>53</sup> and others.

Chemical co-precipitation is another popular synthesis technique. This is a wet chemical method which has advantages such as lower processing temperatures and higher level mixing of precursors when compared to SSR.<sup>54</sup> Co-precipitation involves combining solutions of precursor powders slowly to form a precipitation solution which is agitated, filtered, and aged over time to eventually form a cake of material that is crushed and calcined to yield the final material. This method enables the formation of highly homogeneous and pure phase materials with good sinterability at relatively low temperatures. This is a lengthy process, however, which can take from several hours to days to perform. Li et al.<sup>55</sup> and Zhang et al.<sup>56</sup> report on the use of the co-precipitation method to fabricate different transparent garnet ceramics.

The sol-gel technique is another wet-chemical method with similar positive and negative attributes as chemical co-precipitation. In this process, a colloidal suspension with the ceramic powder is formed along with the slow addition of organic content and heat over time to form a gel-like substance which is subsequently calcined to yield the final material. Dupont and coworkers studied different parameters in the sol-gel process for the preparation of yttria nanopowders.<sup>57</sup> Additionally, Balabanov et al.<sup>58</sup> and Hajizadeh-Oghaz et al.<sup>59</sup> both report on using the sol-gel process to synthesize  $\text{MgAl}_2\text{O}_4$  and  $\text{Y}_2\text{O}_3$  powders, respectively, for transparent ceramic applications.

In flame spray pyrolysis (FSP), a solution of the precursor powders is sprayed into a mist which is heated using a flame causing the solvent to burn off and the resulting material is collected on a substrate. This is a somewhat new and less-utilized process, but enables the relatively rapid and inexpensive formation of highly homogeneous nanopowders.<sup>60</sup> Teoh et al. provides a good review of the FSP technique and applications.<sup>61</sup> Jones et al.<sup>62</sup> and Katz et al.<sup>63</sup> have used FSP synthesis for the fabrication of transparent Nd:YAG and Er:YAG, respectively.

#### **4. Transparent Ceramic Processing Methods**

A variety of techniques currently exist for the processing of transparent ceramics from forming to sintering and post-processing. The ultimate goal of processing is to achieve near full-density ceramic structures with limited scattering sources. There is no one correct way to process transparent ceramics and every method possesses advantages, disadvantages, and applications. The discussion below provides a review on the most commonly utilized processing methods along with examples of research and reports in literature.

Dry-pressing has been a very widely used ceramic forming method for a long time due to its simplicity. Dry-pressing involves filling a die with powder and then uniaxially pressing it with either one or two rams in order to form a relatively dense compacted green structure, as shown schematically in **Figure 2**. Often times, a small amount of binder is added to the powder to aid in the pressing process and provide lubrication between particles, thus enabling improved compaction behavior as well as green mechanical properties.<sup>22</sup> Additionally, powders with an optimized particle size and distribution can improve packing efficiency during pressing.<sup>64-67</sup> For transparent ceramic fabrication, dry-

pressing is typically used in conjunction with cold isostatic pressing (CIP). In CIP, the green ceramic structure is placed into a sealed flexible mold or pouch within an enclosed chamber where uniform (isostatic) pressure is applied via an immersion fluid at room temperature to compact the structure, as depicted in **Figure 3**. This additional process further improves the green body density. CIP can also be used independent of dry-pressing with an unformed powder being used directly.<sup>22</sup> After dry-pressing and CIP, debinding and sintering processes are required. Debinding simply involves heating the ceramic in a furnace up to a temperature which burns off the binder. Pressureless vacuum sintering is the commonly utilized sintering process which involves the use of a heating element in a vacuum chamber. Sintering without vacuum in other atmospheres has been shown to adversely affect grain growth and densification behavior as well as introduce impurities, which is why a vacuum furnace is typically used.<sup>68-70</sup> The temperatures for debinding and sintering depend upon what materials are being used. Zhang et al. and Ge et al. report on highly transparent Ho:YAG and Nd:YAG ceramic pellets, respectively, which were both fabricated using dry-pressing and CIP followed by vacuum sintering.<sup>71-72</sup> Additionally, many of the reports from the previous materials section include dry-pressing, CIP, and vacuum sintering.<sup>32, 42, 49, 73</sup> Overall, dry-pressing and CIP followed by vacuum sintering are simple, consistent, and efficient processes, but do not offer much flexibility in terms of part design since not all shapes can handle being made by dry-pressing and CIP. Furthermore, dies need to be made specifically for individual part designs and cannot be easily modified without additional processes and tooling costs.

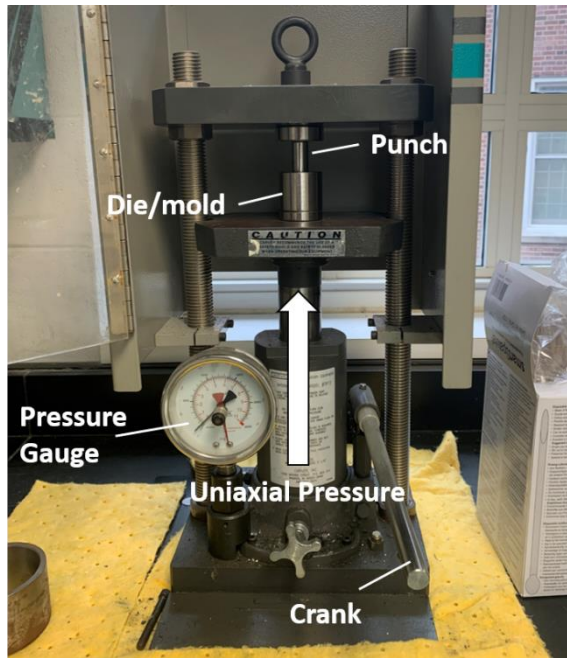


Figure 2. Schematic of a dry-press process.

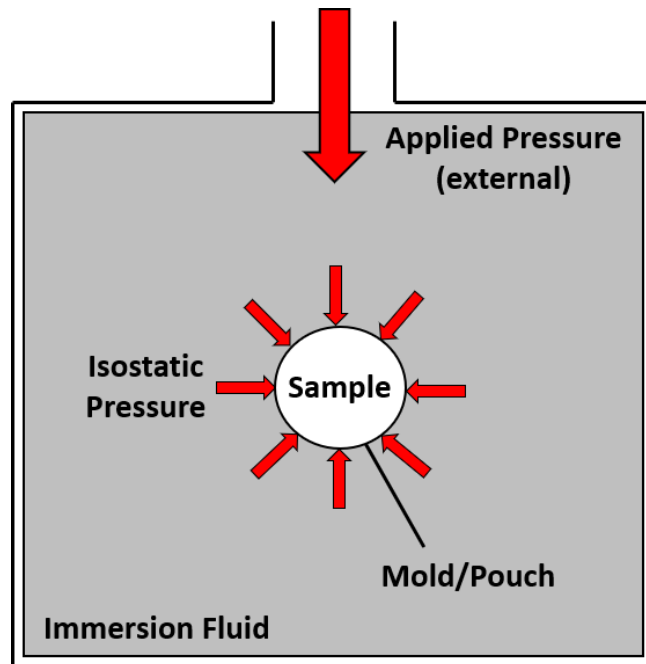


Figure 3. Schematic of a CIP process.

Hot-pressing (HP) is another uniaxial pressing method, but involves the application of heat and pressure to simultaneously form and sinter the ceramic in one step. The HP process typically utilizes a graphite heating element to heat a vacuum chamber which contains a set-up of equipment similar to that in the aforementioned dry-pressing process. As a related process, spark plasma sintering (SPS), also known as field assisted sintering technique (FAST), applies an electrical current directly through a graphite mold as opposed to using a heating element. In this manner, SPS/FAST can enable faster and more efficient processing.<sup>74</sup> Schlup et al. conducted a study on hot-pressing parameters for alumina ceramics and achieved 65.3% in-line transmission in the visible region.<sup>75</sup> Zhang et al. reported on Gd:YAG ceramics fabricated via SPS which achieved in-line transmission values of 77.1% in the visible range and exhibited ultraviolet emission via photoluminescence excitation.<sup>76</sup> Talimian and coworkers also recently conducted a study on SPS parameters and their effect on contamination and discoloration in transparent  $\text{MgAl}_2\text{O}_4$  ceramics.<sup>77</sup> In addition to these studies, some reports in the previous materials section also include SPS.<sup>26, 38, 50</sup> Similar to dry-pressing and CIP, HP and SPS/FAST are limited in the size and shapes of the structures that they can produce. Furthermore, the facilities and technology involved in HP and SPS/FAST are relatively complex, expensive, and require a good understanding of many interconnected parameters. These fabrication methods find advantages in improved efficiency however, due to their shorter processing times which are completed in a single-step as well as a high degree of densification as demonstrated in the reports.

Slip/mold casting, gel casting, and tape casting offer a much different approach to the aforementioned dry processing methods. In general, wet ceramic processing methods can offer improved control of particle-particle interactions, resulting in increased homogeneity and other more desirable properties over dry ceramic processing routes.<sup>78-79</sup> In slip/mold casting, an aqueous ceramic suspension is prepared with additional binders and dispersants and formed into a mold of the desired shape which is allowed to dry over time. This method enables the fabrication of structures of any shape which can be made into a mold. Alternatively, in gel casting, water-soluble monomers are added to the suspension and the mixture is polymerized within a mold. Gel casting has been known to exhibit advantages over slip/mold casting through the production of near-net shape parts

with improved homogeneity and green strength.<sup>78, 80</sup> In tape casting, the ceramic suspension is cast through a “doctor blade” to form a thin sheet or tape. These thin tapes can then be cut, layered, laminated, or pressed together as needed to form the desired structure.<sup>81</sup> These casting processes can also be combined with CIP processing to further increase green density. Once the casted parts are sufficiently dry, they are debinded and then sintered. As with the aforementioned dry-pressing and CIP processes, vacuum sintering is typically employed as the densification method for casted transparent ceramics. Appiagyei et al. reported on slip casted YAG ceramics using an aqueous suspension which was vacuum sintered and achieved transmittance values greater than 80% in the wavelength range from 340 – 800 nm.<sup>82</sup> In a very recent study, Liu et al. reported on using a combination of gel casting, CIP, and vacuum sintering to fabricate transparent  $MgAl_2O_4$  ceramics which achieves good mechanical properties as well as in-line transmittance values of 79.8% at 400 nm and 86.4% at 1064 nm.<sup>83</sup> Jin et al. reported on zirconia-doped yttria ceramics fabricated using tape casting and vacuum sintering which achieves a high in-line transmittance value of 81.7% at 1000 nm.<sup>84</sup> A couple of reports from the previous section also included casting methods to form transparent ceramics.<sup>27, 33</sup> Despite the many advantages of wet processing, there also some disadvantages. Wet processing methods can be complex in terms of proper slurry preparation and require a great understanding of rheological behavior and interactions between particles. Furthermore, the wet processing methods are typically less efficient and take longer due to the additional steps and processes required, such as slurry preparation and drying.

Similar to CIP, hot isostatic pressing (HIP) is a post-sintering treatment method for transparent ceramics; however, HIP is conducted at an elevated temperature with an inert gas as the fluid pressure medium.<sup>22</sup> In this method, the ceramic is initially sintered (sometimes known as pre-sintering), followed by HIP treatment at high temperatures to complete the densification. This combination of processes has been shown to improve the density, microstructure, and optical properties of ceramics.<sup>85-87</sup> Furthermore, since the ceramic is previously sintered, it should have sufficient strength to undergo the HIP treatment without breaking, thus enabling a wide variety of initial forming methods and structures to be compatible with this post-treatment method. Wang et al. reported highly transparent yttria ceramics fabricated using low temperature pre-sintering followed by HIP

treatment which achieves fine grain sizes and 81.7% in-line transmission without the use of sintering additives.<sup>88</sup> Luo et al. also reports on the use of pre-sintering and post HIP treatment to fabricate transparent Co:MgAl<sub>2</sub>O<sub>4</sub> ceramics for eye-safe solid-state laser applications.<sup>89</sup> Some of the aforementioned reports also utilized post HIP treatment.<sup>25, 32,</sup>

73

Following sintering, some transparent ceramic materials may require an annealing process. Sintering processes can introduce defects and residual stresses as well the formation of oxygen vacancies and color centers which produce undesirable results towards achieving high optical quality. Oxygen vacancies are primarily formed due to the reducing atmosphere found within most vacuum furnaces with graphite heating elements. Annealing in air at a high temperature can help fill these oxygen vacancies and relieve residual stresses to improve transmission in optical ceramics. Fu et al. and Zhang et al. both demonstrate improved optical properties through annealing in air in their reports on transparent Nd:YAG.<sup>90-92</sup>

As the final step in nearly all transparent ceramic fabrication processes, thorough polishing is required. The polishing process is necessary to reduce scattering losses due to surface roughness. Achieving a mirror-like finish is the ideal end goal and there are different methods to accomplish quality surface finishes. Most commonly, polyurethane polishing plates and cloth pads are used along with a polishing suspension composed of fine abrasive particles from a material of high hardness, such as diamond. Additionally, abrasive materials like alumina and silica can be used in an alkaline solution to provide an additional chemical polishing effect which can reduce subsurface damage as well; this is known as chem-mechanical polishing (CMP).<sup>93-95</sup> Magnetic field-assisted finishing (MAF) is another alternative technique which utilizes an applied magnetic field and abrasive magnetic particles to polish. The MAF process offers more precise and controlled polishing over the more conventional methods for optics.<sup>95-96</sup>

## **B. 3D Printing of Ceramics**

### **1. Background**

Additive manufacturing (AM), also known as 3D printing, is a general term used to describe the fabrication of a physical part from a digital 3D model by the successive addition of material.<sup>97</sup> In this process, a 3D computer-aided design (CAD) model is transformed into a “stereolithography” (.stl) file where it is approximated by small triangles and then “sliced” into a series of 2D cross-sections that are built upon one another at specified thicknesses to form the final part.<sup>98-99</sup> 3D printing enables the fabrication of a wide array of controllably complex structures that might otherwise be difficult or even impossible to make.<sup>97, 100</sup> Parts can be formed in either a point-by-point, line-by-line, or layer-by-layer manner and post-processing may or may not be necessary depending upon the materials and techniques chosen.<sup>100</sup>

AM is considered to be a relatively new process and is significantly different than more traditional subtractive or equivalent manufacturing processes such as machining or casting, respectively, which have been used for hundreds of years.<sup>98, 100-101</sup> Some of the first AM technology was developed in the 1980’s in the form of stereolithography by Charles Hull and 3D Systems, Inc. and has been regarded as a manufacturing revolution, garnering significant attention around the world.<sup>97, 99-100</sup> Originally, AM technology was developed with the focus being on flexibility of design, prototyping, and reducing the time-to-market for new products.<sup>97-98, 101</sup> Due to significant research and technological advancements, including 3D modelling, computer numeric control (CNC), and others, AM has become a method that is used worldwide to produce highly complex and customizable products with excellent properties that are unable to be made using any other method.<sup>98, 101-102</sup>

Currently, 3D printing is integrated into many different industries such as biomaterials, pharmaceutical, aerospace, automotive, architecture, and others and has become so accessible that simple instruments can even be purchased in the low thousand or even hundred US dollar range for personal use in homes.<sup>102</sup> 3D printing has become widely used because of the many attractive attributes it possesses. In the past, it would be necessary to have experienced workers with a great understanding of different machinery, tools, and materials in order to fabricate customized parts.<sup>102</sup> AM technology reduces the

tooling and labor costs associated with making customized parts through its flexible and autonomous nature while also making it possible to quickly and easily modify the design of a part using modeling software. Furthermore, it is possible to fabricate parts of very small geometries to a fine degree of precision due to the high resolution of modern AM technology. Finally, the additive nature of 3D printing enables materials, energy, and costs savings since there is little to no waste material and structures can be intelligently designed with controlled porosity to limit material use while maintaining desired properties.<sup>97</sup> With all of these benefits possible from AM technology, the strategies of production and business can be changed to create entirely new products with different functionalities or improve upon existing ones.<sup>101</sup>

Thus far, the primary materials that have seen success when used for 3D printing have been polymers and metals.<sup>100-101</sup> However, in recent years, ceramic materials have made their way into the 3D printing world. The first reports of AM with ceramic materials were published in the 1990's by Marcus<sup>100, 103</sup> and Sachs.<sup>100, 104</sup> Since then, there has been some steady development in ceramic AM, including techniques specific to ceramics. Ceramics are of interest for applications in a variety of fields and can be characterized by their excellent thermal and chemical stability, hardness, high mechanical strength, as well as optical and electrical properties. The combination of 3D printing technology with ceramic materials opens a door for many potential opportunities.<sup>100-101</sup> However, AM of ceramics poses many challenges due to inherent processing requirements and the fact not every AM technology can be utilized to produce ceramics.<sup>101</sup> So, despite the progress that has been made so far, AM of ceramics remains relatively underdeveloped, leaving significant research and development efforts to fully enable the potential of ceramic AM.

## **2. Methods and Technologies**

A variety of AM technologies currently exist and can be classified by feedstock among dry powders, slurries, and bulk-solids. Despite being relatively new, ceramic AM technology is still largely based upon traditional ceramic processing practice and techniques.<sup>100-101</sup> Below is a review of the most commonly used AM technologies today along with their attributes and applications. Schematics of some of the AM technologies are presented in **Figure 4** (adapted from Zocca et al.<sup>101</sup>) and a brief overview of the different AM technologies is presented at the end of this section in **Table 2**.

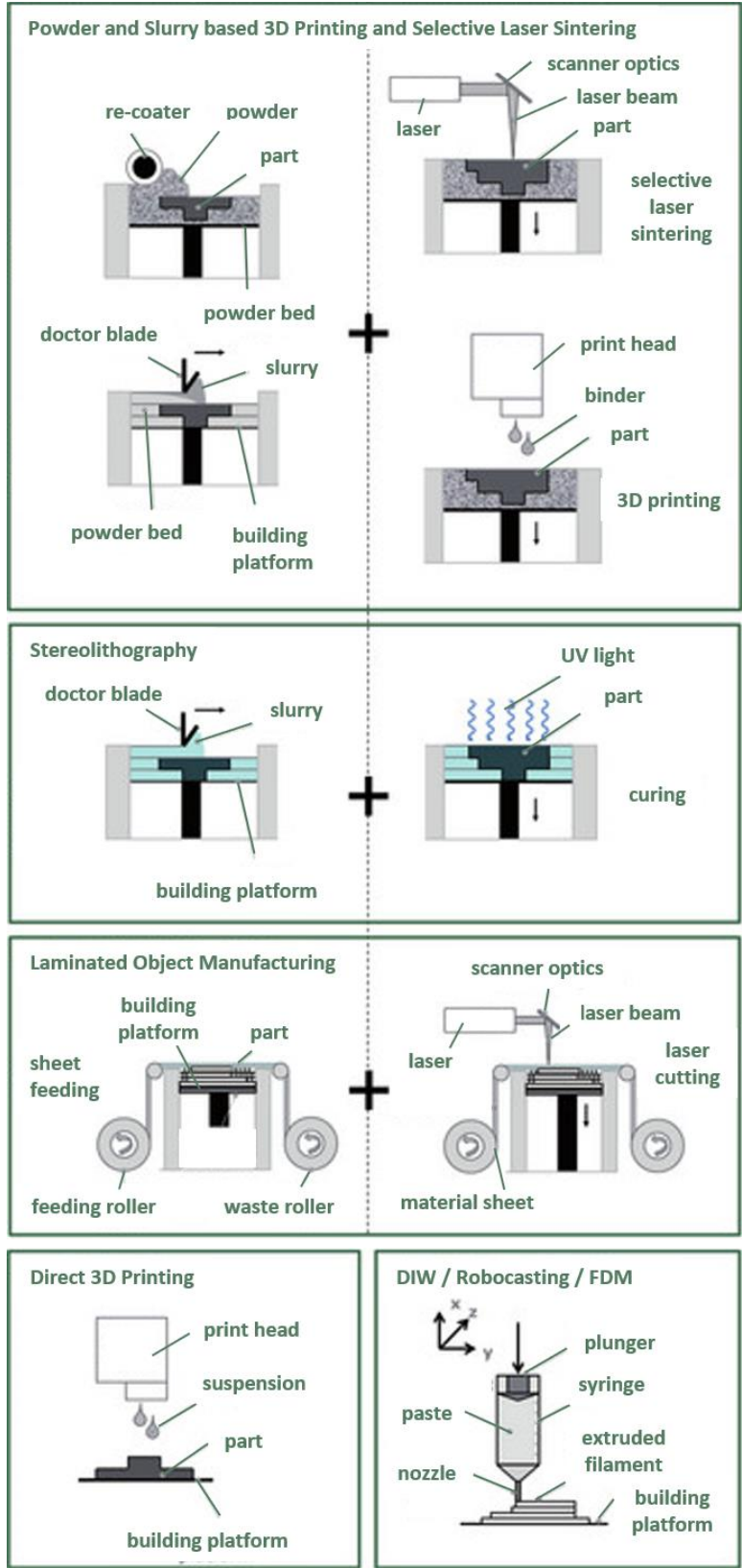


Figure 4. Schematics of popular AM techniques, adapted from Zocca, Colombo, Gomes, and Günster .<sup>96</sup>

### **a. Slurry Methods**

In slurry-based AM techniques, ceramic particles are typically suspended in an aqueous medium which may include other additives such as dispersants, binders, plasticizers, and photopolymers. Depending on the application and specific technique, the slurry can vary greatly in both composition and rheology. In general, slurries will vary between approximately 30-60 vol% solids-loading and have viscosities on the order of mPa·s to Pa·s. In order to obtain the best results, it is necessary to develop a well-balanced and stable slurry which fits the needs of the technique chosen and the final application. The mechanical properties of parts fabricated using slurry-based techniques are typically superior to powder-based techniques due to improved particle-particle interactions and packing.<sup>100</sup>

First developed in 1997 by Cesarano and coworkers<sup>105-106</sup>, direct ink writing (DIW), also referred to by other names such as robocasting (RC), is a general term used to describe techniques that involve a highly viscous ink or paste being extruded as a filament through a moving nozzle at room temperature. This enables the fabrication of large as well as micron-scale complex parts that experience great shape retention without typically utilizing any sort of built-in support structures.<sup>107-109</sup> The main parameters of interest in this process are the rheological properties and behavior of the suspension and the nozzle size.<sup>97</sup> DIW commonly exhibits issues with porosity, poor surface quality, and poor adhesion between layers, however.<sup>97, 100</sup> Therefore, this technology is not always implemented for dense engineering ceramics, but more commonly for porous ceramic structures that do not require high surface quality or resolution. Currently, this technology is being used for applications such as medical implants and tissue engineering,<sup>110-116</sup> filters,<sup>117-118</sup> energy devices,<sup>119-120</sup> and others.<sup>100</sup>

As related technologies to DIW, inkjet printing (IJP) and contour crafting (CC) utilize a similar process. IJP was first developed for ceramics by Blazdell and coworkers in 1995 and utilizes small computer controlled printheads to deposit a slurry onto a substrate in either a continuous or drop on demand (DOD) mode.<sup>121-122</sup> The resulting parts are highly dependent on the rheological behavior of the slurry and the printing parameters.<sup>97, 100</sup> Parts are typically limited to small and simple shapes due to the droplets being mere nanoliters in size and the method being incapable of producing overhanging or

hollow structures. IJP finds most of its applications in thin functional layers and microelectronics.<sup>97, 100, 102</sup> On the other hand, CC resembles an automated version of a very traditional technique used in pottery. The process uses a viscous clay blend that is deposited through a nozzle onto a surface that is subsequently flattened to size using a spatula.<sup>102</sup> This technique utilizes very large nozzle sizes and high pressures which is what separates it from DIW and IJP. For these reasons, CC is typically applied for large-scale parts in construction. Although mainly used with cement, there have been some uses of CC for ceramics. In construction, CC offers the ability for unique design options not typically attainable due to equipment constraints as well as on-site construction with local materials.<sup>97</sup>

Stereolithography (SL, STL, or SLA) is one of the oldest as well as widely used AM techniques and was first developed in the 1980s by Charles Hull and 3D Systems Inc.<sup>97, 99-100, 123</sup> SL and related technologies are unique in their use of pre-ceramic polymers (PCPs), which are suspensions composed of photocurable polymers and ceramic particles. In SL, a build plate is submerged the distance of one layer into a vat containing the PCP which is selectively cured (solidified) point-by-point using a UV laser through a process known as photopolymerization. Once an entire layer is cured, the build plate is again moved the distance of one layer and the process repeats until finished. After the part is done printing, any excess material is removed. Afterwards, the part may undergo additional curing, pyrolysis, and other post-processing steps. The finished part is referred to as a polymer derived ceramic (PDC).<sup>97, 99-100, 124-126</sup> Parts fabricated by SL exhibit high surface quality along with fine features down to a micron scale. To achieve such surface quality and micron scale features, many parameters must be taken into consideration. The suspension must possess well-dispersed ceramic particles that do not have greater light absorption than the polymeric medium as well as exhibit long-term stability and suitable viscosity for printing. Furthermore, the exposure period of the laser must be fine-tuned to prevent over- or under-curing. For these reasons, SL is a relatively complicated, expensive, and slow technique with very limited materials selection. Due to their high performance, quality, and fine resolution, however, PDC parts created via SL are widely used for complex, small-scale structures, such as in microelectronic components,<sup>127-128</sup> bone tissue engineering,<sup>129-130</sup> and many other technologies.<sup>97, 99-100</sup>

As related methods to SL, digital light processing (DLP) and two-photon polymerization (TPP) offer slight variations to the photopolymerization process. DLP uses thousands of digital micromirror devices (DMDs) to form a patterned mask or projection screen which exposes the light source to only certain areas on the build plate. This allows for a single layer to be cured all at once and therefore is a significant improvement in terms of process efficiency when compared to SL while still maintaining micron-scale resolution. This technique has been demonstrated for fabricating high density ceramics and PDCs with mechanical properties comparable to that of conventionally prepared ceramics.<sup>131</sup> DLP has been primarily used in the fabrication of fine-featured structures, such as metamaterials, heat exchangers,<sup>132</sup> piezoelectric devices,<sup>133</sup> and other technologies.<sup>100</sup> Alternatively, in TPP, polymerization is initiated by the absorption of 2 photons from a high-intensity near-infrared or green laser source in a submicron volume. In SL and DLP, only one photon is used, and polymerization only takes place on the surface. In this way, TPP process enables parts to be fabricated that would be impossible via SL or DLP.<sup>134</sup> Currently, TPP is limited to transparent PCP slurries as feedstock, and has been demonstrated in the fabrication of high-quality ceramic structures at scales as small as nanometers.<sup>135-142</sup> TPP suffers from longer processing times as well as the inability to produce large-scale parts.<sup>100</sup>

### **b. Powder Methods**

In powder-based techniques, a loose ceramic powder is typically laid out as a bed which acts as a support structure to build parts upon. The powder can be bonded together and formed into a layer in different ways, depending upon the technique chosen. The bonding step in this process is the main source of cost and complexity and there are many considerations to make. After a layer is formed, a fresh bed of powder is added for the next layer, and the process continues until the part is finished followed by the removal of excess powder.<sup>100</sup> Due to the presence of the powder bed, it is not necessary to design support structures for the part. In general, parts fabricated via dry powder techniques tend to be more porous and have weaker mechanical properties than those fabricated via slurry techniques, especially when a binder is used as the fusion source.<sup>97, 100</sup> The porosity and weak mechanical properties can be reduced or even alleviated, however, with proper processing to achieve a good particle size and distribution and maximize packing which can also lead to greater resolution.<sup>97, 99, 143</sup>

Patented in 1986 by Deckard and Beaman,<sup>144</sup> selective laser sintering (SLS) is a highly complex and challenging process due to the different mechanisms and interactions that must be considered. The first reports for the use of SLS for ceramics were made by Lakshminarayan and coworkers in 1990 at the University of Texas at Austin.<sup>100, 145-146</sup> SLS utilizes a carbon dioxide laser to selectively heat the surface of the powder bed to the point of sintering at specific locations, thus joining the particles together and forming a layer.<sup>99-</sup><sup>100</sup> Due to the refractory nature of ceramics, a very high-powered laser with sufficient exposure time is necessary to properly sinter the particles. This can be difficult and time consuming to achieve, therefore it is more common to mix in other materials which act as sintering aids, fluxes, and binders that form a glassy phase within the part.<sup>100</sup> SLS accommodates a broad range of ceramic materials and is capable of producing high-quality parts with good mechanical properties when the material and process parameters are finely tuned and supporting processes are included.<sup>99</sup> Using SLS alone, ceramic parts are fabricated with less than 50% of theoretical density due to significant porosity and exhibit high shrinkage. By performing additional infiltration and isostatic pressing to compliment the SLS process, it is possible to achieve densities as high as 94% of theoretical, as demonstrated by Shahzad et al.<sup>100, 147-152</sup> Processing and material parameters highly effect the properties of the resulting part as well. In general, it is preferred to use micron-sized powders of spherical shape that are homogeneously coated with a small amount of binder and contained in an inert atmosphere. SLS suffers intrinsically from poor resolution and surface quality and is incapable of producing full density parts. Due to all of this, SLS is a relatively costly and time-consuming process but has found application in the aerospace and medical industries to fabricate controllably porous and complex structures.<sup>99-100</sup>

Selective laser melting (SLM) is similar to SLS and was first developed by the Fraunhofer Institute of Laser Technology in 1996.<sup>153</sup> SLM is a single-step process where the powder bed is selectively irradiated by a laser and is fully melted without the use of a secondary phase, such as a binder. As mentioned previously, ceramics have very high melting points which makes this process difficult and expensive due to the high-energy laser requirements. For this reason, SLM has not seen much development in the field of ceramics.<sup>100</sup> The benefits of this technique are that it is currently the only AM method which is theoretically capable of producing near full density and homogeneous parts that

are ready to use in a single step. SLM not only allows for time savings due to the lack of additional processing, but also results in highly pure parts due to the lack of additional materials.<sup>97, 100, 154</sup> In practice however, SLM alone has not been very successful in achieving fully-dense and high quality parts in a single step due to challenges in properly tuning the process and laser parameters to ensure sufficient melting, and, due to thermal stresses associated with the rapid heating and cooling, results in structural problems in the fabricated parts.<sup>100, 155-158</sup> Some additional techniques have been proposed to improve upon SLM, such as preheating the powder to help reduce thermal stresses<sup>159-160</sup> as well as different technologies such as laser micro sintering (LMS)<sup>161-162</sup>, LENS<sup>TM</sup> (covered next in this review), and slurry-SLM which are all directly based on SLM. For the aforementioned reasons, SLM is not necessarily a method of choice for manufacturing ceramic materials. More research and development are required to solve the problems associated with SLM before this technology will be more commonly used in the ceramic industry. However, SLM technology has found some use for producing ceramic medical implants.<sup>99-100, 160, 163</sup>

Directed energy deposition (DED) is a technique which goes by many names, such as laser engineered net shaping (LENS<sup>TM</sup>) and others. DED/LENS<sup>TM</sup> is essentially an extension of the SLM technique described earlier that was developed to help increase the density of parts and reduce defects.<sup>100</sup> In DED a powdered feedstock material as well as the substrate are melted by a high-power laser and injected onto a substrate.<sup>97, 99</sup> The injected material fuses with the substrate and solidifies upon cooling to form the part.<sup>97, 100, 124, 164</sup> This is slightly different than SLM in that no powder bed is utilized and the feedstock material is melted prior to being injected.<sup>97</sup> Although this technology is mostly used for metals and alloys, there have been a number of successful demonstrations with ceramics too.<sup>99-100, 165-167</sup> DED technology has the advantages of relatively high printing speeds and the capability of fabricating large (meter-scale) parts with strong mechanical properties. Furthermore, DED can print with multiple materials at the same time as well as across multiple axes and can be combined easily with subtractive machining to have a more complete process. However, DED typically suffers from its inability to create parts of high complexity or surface quality. DED is primarily applied in the aerospace and automotive industries for repairing parts and other applications.<sup>97</sup>

Not to be confused with the general term “3D Printing”, three-dimensional printing (3DP™), sometimes referred to as binder-jetting, is a specific technique which was licensed by MIT in 1989.<sup>99-100</sup> 3DP was first developed by Sachs et al. at MIT, but was not developed for ceramics until later in the 1990’s.<sup>100-101</sup> In 3DP, an aqueous organic binder solution is sprayed through print heads onto specific regions of the powder bed.<sup>99</sup> The powder is bound together by the solution and then solidifies to form a layer.<sup>99-101, 124</sup> 3DP is more simple and affordable than the other powder methods and is a good alternative for when the powder material being used has a very high melting point or using high powered lasers is not an option.<sup>97</sup> 3DP offers the ability to use a wide variety of ceramic materials to produce a range of both large and small structures without requiring integrated supports.<sup>99-100</sup> To achieve a high-quality part, it is necessary to optimize the rheology of the binder, process/printing parameters, and properties of the ceramic powder.<sup>97, 143</sup> In general, one should use a binder with molecular weight less than 15,000 and a fine ceramic powder with spherical-shaped particles for optimum performance.<sup>97, 100</sup> The main drawbacks of 3DP are that it tends to produce parts with low resolution and poor surface quality.<sup>100</sup> Furthermore, 3DP suffers from high porosity and weak mechanical properties.<sup>97</sup> For these reasons, 3DP is not typically employed for high-performance or advanced structural ceramics, but has found use primarily in the medical industry for applications that require parts which are not fully-dense.<sup>100, 168-169</sup>

### **c. Bulk-Solid Methods**

Bulk-solid technologies include solid feedstocks that are not in powder form. Due to the brittle nature of ceramics, it may be necessary to use composite feedstocks which possess properties that enable printing. In general, bulk-solid techniques tend to produce parts of large size and increased mechanical properties, but suffer from limited material selection and the inability to produce fine and complex structures.

Fused deposition modeling (FDM) is the most widely used AM technique and has the largest shipment of units around the world. Although it was originally developed for polymers by Crump et al. in 1992,<sup>170</sup> it was first reported for the use of ceramics in 1995 by Yardimci et al. at Rutgers University.<sup>171</sup> The FDM process uses composite filaments composed of thermoplastic binders which are highly-loaded with ceramic particles.<sup>100</sup> This filament material is then heated to a semi-liquid state until it is able to be extruded through

a nozzle and deposited onto a platform where it solidifies to form a layer. For smooth and quality printing, the ceramic-to-binder ratio, dispersity, and particle size and distribution should be optimized to achieve a viscosity in the range of 10 to 100 Pa·s. Furthermore, the layer thickness as well as the width and orientation of the filament highly affects the resulting mechanical properties.<sup>97, 99-100, 172</sup> The main appeal with this technology comes with its flexibility of machine/unit size, the low cost of equipment and materials, and the overall fast and simple building process.<sup>97, 99-100, 124</sup> The FDM process suffers from the limited selection of thermoplastic materials as well as poor surface quality and resolution, interlayer distortion, and weak mechanical properties.<sup>97, 99-100, 172-173</sup>

Laminated Object Manufacturing (LOM) was originally developed for paper, plastics, and metals, yet was first reported on for the fabrication of ceramic parts by Griffin et al. in 1994.<sup>174</sup> Technically speaking, LOM is a combination of subtractive and additive manufacturing processes, but will be considered as a 3D printing technique for the purpose of this review.<sup>100</sup> In LOM, a laser or mechanical cutter is used to cut previously prepared thin sheets of materials which are coated with thermal adhesive agents. The layers are stacked on top of each other and bound together (laminated) by the application of heat and pressure.<sup>99-100</sup> Excess material is typically left as support throughout the process and is removed at the end.<sup>97, 164</sup> LOM has been shown to be very successful in creating high density parts with little to no deformation with a microstructure comparable to that of ceramics prepared by conventional methods.<sup>100</sup> This process is not very costly and works well for fabricating large and simple structures.<sup>99</sup> LOM is limited, by the inability to create small features or complex shapes and can suffer from interlayer delamination, interfacial anisotropy, and low dimensional accuracy and surface quality.<sup>97, 100</sup> Furthermore, parts fabricated via LOM have been demonstrated to have highly anisotropic properties depending on the orientation of the part.<sup>175</sup> Also, due to the intrinsic subtractive nature of this process, some material and time is wasted in cutting the layers and excess material.<sup>97, 99, 124</sup> Due to the recent demand of complex ceramic structures, development and use of LOM has been relatively limited.<sup>100</sup>

Table 2. Overview of Popular AM Technologies.

Method	Feedstock	Mechanisms	Resolution	Applications	Notes	References & Reports
<b>DIW</b>	Slurry	Extrusion	10 $\mu$ m-mm	Structural components, porous ceramics	-Simple, cheap, quick -Low quality and poor properties	20, 92, 95, 100-115
<b>IJP</b>	Slurry	Extrusion (droplets)	10 $\mu$ m-mm	Thin layers, small electronics	-Slow, limited in size/shape of parts	92, 95, 97, 116, 117
<b>CC</b>	Slurry	Extrusion	mm-cm	Large structures	-Good mechanical properties	92, 97
<b>SL</b>	Slurry (photo-active)	Polymerization	1-100 $\mu$ m	Small, complex structures	-High quality parts -Complex, slow, expensive	92, 94, 95, 118-125
<b>DLP</b>	Slurry (photo-active)	Polymerization (photo mask)	1-100 $\mu$ m	Small, complex structures	-More efficient and similar quality to SL	95, 126-128
<b>TPP</b>	Slurry (photo-active)	Polymerization (two photons)	nm- $\mu$ m	Small, functional ceramics	-Very high resolution -Long process, limited to small parts	95, 129-137
<b>SLS</b>	Powder	Sintering	100 $\mu$ m-mm	Porous ceramics	-Complex and expensive -Needs supporting processes	94, 95, 139-147
<b>SLM</b>	Powder	Melting/fusion	100 $\mu$ m-mm	Structural parts	-Complex and expensive -Not desirable for refractory materials	92, 95, 148-158
<b>DED</b>	Powder	Melting, extrusion	250 $\mu$ m-mm	Large structures	-Improved from SLM	92, 94, 95, 119, 159-162, 183
<b>3DP</b>	Powder	Binder jetting	50 $\mu$ m-mm	Lightweight and porous parts	-Simple and versatile -Lacking mechanical properties	92, 94-96, 119, 138, 163, 164
<b>FDM</b>	Bulk-solid (composite filaments)	Extrusion	100 $\mu$ m-mm	Functional composites	-Cheap and quick -Limited materials, poor quality parts	92, 94, 95, 119, 165-168
<b>LOM</b>	Bulk-solid	Cutting, lamination	100 $\mu$ m-mm	Large structures	-Anisotropic properties, limited complexity	92, 94, 95, 119, 159, 169, 170

### **3. Current State and Future of Ceramic 3D Printing**

AM technology of the present day has some clear advantages as well as disadvantages when compared to conventional manufacturing methods. The recent demand for highly complex ceramic parts for various applications has led to research and development in the field of AM technologies with the goal of optimizing the process to maximize the many benefits that AM presents. AM technology has grown and changed rapidly in the past few decades, which makes it difficult to predict what state it will eventually attain in the future. With current trends in development, however, it is predicted that AM technology will continue to merge with conventional subtractive and equivalent manufacturing and eventually even become more valuable to industry than either of the two.<sup>98</sup> In recent years, AM technology has become more widely accepted, affordable, and user-friendly to the point where the general public can have success operating a 3D printer without extensive training or experience and possibly even own one in their own home.<sup>97-98, 102</sup> This assimilation of AM technology into industry as well as society is important as the exposure will hopefully spark interest and attention towards future progress. Although it is not clear where AM technology will be years from now, there are certainly predictions and considerations that can and should be made.

The aerospace and medical industries are currently some of the heaviest users of ceramic AM technology and illustrate significant promise for the future of this field.<sup>97</sup> Aircraft and other vehicles require parts with high strength-to-weight ratios and complex cross-sections that can also withstand high temperatures and are resistant to corrosion, which makes 3D printing as well as ceramics a great fit.<sup>97, 99, 176</sup> Ultra-high temperature ceramic and ceramic composite components are already commonly used in the aerospace industry and the implementation of AM technology has and can continue to advance the aerospace field. Another area that is of specific interest within the aerospace industry is spare parts and repair. Repairing aircraft and vehicles can be very inefficient in terms of cost and time, particularly if the required part is very old or complex and only a small number of the part is needed.<sup>99</sup> Using modeling software, it is possible to design spare parts that are outdated or no longer available which could drastically affect the spare parts supply chain and repair markets. Furthermore, it is costly for a company to keep spare parts

and equipment in their inventory just in case there is a need; with AM technology, the part can be produced as needed.<sup>100, 176</sup>

In the medical industry, ceramic AM technology has been nearly essential for bone scaffolds, tissue engineering, implants, and other patient-specific custom products.<sup>97, 177</sup> Through scanning and modeling, nearly perfect prosthetics and replacement parts can be made which improves the insertion process as well as the patients adjustment to the part, recovery time, and overall functionality.<sup>99, 178</sup> AM can even be useful for surgeries where doctors can create physical models which are used to prepare and practice ahead of time.<sup>97, 99, 179-180</sup> These models can be shared among different doctors and researchers relatively quickly and easily to ensure that the design is proper and make any adjustments that are necessary.<sup>97</sup> Finally, the controlled porosity of ceramics fabricated via AM technology is essential for bone ingrowth and proper stiffness and strength in implants.<sup>99, 181</sup> All of the aforementioned attributes explain how AM technology yields parts which enable faster and easier operations with better results both functionally and cosmetically than those produced via other methods.<sup>99, 182-184</sup> There are some drawbacks that limit progress in this field, such as difficulties in adhering to the FDA.<sup>97, 185-186</sup> Furthermore, there are material issues from a bio- and machine-compatibility perspective. Since not all ceramics are appropriate as biomaterials, and not necessarily all biomaterials can be printable, there are fairly limited options for material selection.<sup>97, 187</sup>

From a production standpoint, AM is not currently comparable to conventional methods for mass production and may not be for some years without changes in perspective or technological development. Mass production is different from mass customization (large amount of parts unique from each other), in which 3D printing has a significant advantage over conventional technology.<sup>97</sup> According to a study conducted on producing identical parts using conventional and 3D printing technology, the 3D printed parts were approximately 10 times more expensive per part. Furthermore, when incorporating the tooling and set-up costs to fabricate the parts with conventional technology, the 3D printed parts were only more cost-effective in smaller volumes (27 parts or less) after which the conventional technologies became cheaper to maintain production.<sup>102</sup> So, in order to reap the benefits of AM technology, it is necessary to step back and reconsider how to design, create, and use parts from a different point of view without concern about conventional

limitations or how things have always been done.<sup>98</sup> Maximizing materials and energy savings in the future through innovative design will not only improve individual businesses but also have positive environmental and societal impacts as well. Realistically, it is unreasonable to assume that 3D printing will dominate all manufacturing, but ideally, companies of the future will find ways to implement AM together with conventional manufacturing where they are best suited for optimal efficiency. Such strategy is even being implemented at some companies currently.<sup>98</sup> Ultimately, the significant economic benefits of AM are dependent on innovative design and implementation strategies.

### **C. Aims of this Work**

As has been discussed within the literature review of this thesis, both transparent ceramics and 3D printing technology are exciting fields of research which have received significant interest in recent years and have great potential for the future. The combination of these technologies has the potential to yield very interesting and useful results in terms of producing customizable transparent ceramic structures. The combination of these technologies can be used for a variety of applications, such as in the military, defense, and aerospace industries for armor, windows, domes, laser devices, and more. Due to ceramic AM technology being relatively under researched and developed, it has been inherently difficult to produce high quality and fully-dense structural ceramics; however, AM technology currently has significant use for manufacturing porous and/or hollow structures. For the fabrication of transparent ceramics, it is absolutely necessary that the structure be as dense as possible with minimal defects, pores, impurities, secondary phases, and surface roughness. These requirements create challenges towards realizing the benefits of combining 3D printing as a forming method for transparent ceramics. In the literature, there have been some, but very few, reports on 3D printing with optical ceramic materials such as Jones et al.<sup>62</sup> who fabricated transparent YAG laser ceramics via DIW as well as Pappas et al.<sup>188</sup> who used DED to fabricate transparent  $\text{MgAl}_2\text{O}_4$  ceramics. These reports on 3D printing of transparent ceramics do not demonstrate the formation of complex shapes, and utilize either complex and expensive processes (DED) or require significant treatment process like CIP and post-HIP to achieve the reported results.

The goal of the research effort reported in this thesis is two-fold. First, these efforts are undertaken to demonstrate that 3D printing technology can be used to fabricate transparent ceramics with additional characteristic benefits of simple and efficient production of complex structures of varying shapes and sizes. Second, this work will compare the 3D printed transparent ceramics to more conventional transparent ceramic forming methods, such as CIP, processed in a similar way to determine if there is a significant difference in quality and properties. To achieve these goals, green ceramic bodies will be formed of varying shapes and sizes using an alumina slurry along with the Hyrel System 30M 3D printer and EMO-25 extruder, which is a DIW technology. Slurry and 3D printing parameters will be optimized to yield the best quality parts and post-processing steps will be established to achieve transparency in the fabricated ceramics. Additionally, CIP ceramics will be formed and processed under nearly identical conditions as a comparison. Finally, testing and characterization will be performed on all samples to evaluate quality and properties.

## **II. STARTING MATERIALS AND SLURRY PREPARATION**

### **A. Introduction**

Fabricating ceramics which can achieve transparency begins with high quality starting materials. Impurities and improperly processed powders can inhibit densification as well as introduce undesirable scattering sources. Therefore, it is critical to select highly pure powders for starting materials. For these reasons, Baikalex High Purity CR 10D  $\text{Al}_2\text{O}_3$  with 625 ppm MgO was the powder of choice. In this case, the additional MgO is a sintering aid that is known to enhance densification and suppress grain growth, which is desirable for transparent ceramic processing.<sup>22</sup>

Using the alumina powder, a slurry is prepared that is suitable for 3D printing with the Hyrel System 30M and EMO-25 extruder. Slurry preparation requires the use of a medium, in this case deionized (DI) water, as well as additives, such as binders and dispersants, to achieve desirable rheological behavior. In this work, Kuraray ISOBAM™-104 was used, which is an alkaline hydrosoluble copolymer of isobutylene and maleic anhydride that has previously demonstrated success in transparent ceramic processing and

is notable for its multifunctional use as both a binder and dispersant in a variety of applications.<sup>189-194</sup> Similarly, CIP processing also typically requires the use of a binder. In this case, PVA was chosen, since it is a commonly used binder for pressing applications due to its ability to improve compaction and mechanical properties in formed parts.<sup>64-67</sup> After forming, it is necessary that these organic materials be removed prior to sintering through a “debinding” process which is discussed later in the post-processing sections.

These investigations have been conducted to characterize the raw alumina powder for slurry and CIP processing as well as establish “printable” slurry parameters. The powder is evaluated for phase purity, specific surface area (SSA), and particle size and distribution with slurries evaluated for rheological properties both quantitatively and qualitatively with relation to the desired printing behavior.

## **B. Experimental Procedure**

The raw BaikaloX High Purity CR 10D Al<sub>2</sub>O<sub>3</sub> powder was ball-milled in ethanol using high purity zirconia milling media for 24 hours to achieve a fine particle size. After 24 hours of milling, the powder was dried for 24 hours to form a solid cake which was crushed via a mortar and pestle to obtain a usable powder. The obtained powder was characterized via X-ray diffraction (XRD) using a Bruker D2 Phaser X-Ray Diffractometer. The measurement was conducted using Cu k-alpha radiation (30 kV, 10 mA) with a start and end angle of 10° and 75° 2θ, respectively, step size of 0.02° 2θ, and count time of 0.3s. The results were then analyzed using the MDI Jade 9 and PDF-4<sup>+</sup> software as well as the ICDD database for phase identification. The powder was further characterized for specific surface area (SSA) using the Brunauer-Emmet-Teller (BET) method and a Micromeritics FlowPrep 060 to first de-gas the sample for 10 minutes at room temperature, 1 hour at 150°C, and another 10 minutes at room temperature followed by performing the measurement using a Micromeritics Gemini VII. The powder was characterized for particle size (diameter) and distribution via preparation of an approximately 4 vol% solids-loading slurry dispersed with Darvan C which was measured using a Micromeritics SediGraph III PLUS. To accompany the particle size and distribution data, a representative image of the powder was taken using an FEI Quanta

200F Scanning Electron Microscope with secondary electrons to show the particle size and morphology.

For evaluating 3D printing rheology, multiple ceramic slurries were prepared with varying proportions of batch ingredients according to the following recipe: 68-74 weight percent (wt.%) Baikalox High Purity CR 10D Al<sub>2</sub>O<sub>3</sub> powder with 625 ppm MgO, 26-32 wt% DI H<sub>2</sub>O, and 0.4-1.0 wt% ISOBAM™-104 per mixed Al<sub>2</sub>O<sub>3</sub> powder. The aforementioned range of batch ingredients was based upon preliminary research efforts as well as review of similar work in literature.<sup>62, 195-196</sup> The alumina/water and isobam content were incrementally varied to experiment with the effect of each on the resulting rheological properties of the slurry. In one set of batch recipes, the isobam content was held constant at 0.7 wt% per mixed alumina powder, while the alumina content was varied in increments of 2 wt% between 68-74 wt%. In another set of batch recipes, the alumina content was held constant at 72 wt%, while the isobam content was varied in increments of 0.3 wt% per mixed alumina powder from 0.4-1.0 wt%. The slurries were prepared by combining the batch ingredients in a shear mixer until a viscous paste was formed. Zirconia milling media of about 1 cm diameter was then added to the milling jar and the jar was placed in an MTI Corporation SFM-1 Desk-Top Planetary Ball Miller for 1 - 1.5 hours. Once milled, the slurry was loaded into a shear mixer within a customized vacuum chamber to de-gas for at least 15 minutes, or until the air bubbles were removed.

Following de-gassing, the prepared slurry was loaded onto the measurement plate of a TA Instruments Discovery HR-2 Hybrid Rheometer. Observations regarding the flow behavior and shape retention of the slurry were made during the loading process. Measurements on the rheometer were conducted at room temperature under the flow sweep procedure at shear rates from 0.01 – 100 s<sup>-1</sup> using a 40 mm parallel plate geometry to obtain curves of viscosity as a function of shear rate. Flow behavior was calculated directly from the curve of viscosity as a function of shear rate using the power law function:

$$\eta = K\dot{\gamma}^{(n-1)} \quad (1)$$

where  $\eta$  is the viscosity,  $\dot{\gamma}$  is the shear rate, K is the consistency index (viscosity at  $\dot{\gamma}=1$ ), and n is the power law index (also known as flow index). Different flow index values correspond to different flow behaviors: n equal to 1 is Newtonian, n greater than 1 is shear thickening, and n less than 1 is shear thinning.<sup>197-198</sup>

### C. Results and Discussion

The XRD measurement for the prepared BaikaloX CR 10D Al<sub>2</sub>O<sub>3</sub> powder is shown in **Figure 5** along with the pattern for PDF #04-015-8996 which was obtained through the search and match tools using the MDI Jade 9 and PDF-4<sup>+</sup> software/database. This PDF card corresponds to a synthetic corundum ( $\alpha$ -Al<sub>2</sub>O<sub>3</sub>). It can be seen from the figure that the two diffraction patterns are nearly identical with no detectable second phases, indicating that the prepared powder is of a single  $\alpha$ -Al<sub>2</sub>O<sub>3</sub> phase. Since the amount of MgO in the powder (625 ppm) is well below the detection limits of XRD, no secondary MgO XRD lines were observed. BET measurements reported that the specific surface area of the prepared powder was  $7.9571 \pm 0.1174$  m<sup>2</sup>/g. The particle size and distribution data are presented in **Figure 6**. The D10, D50, and D90 represent the mass-percentage of particles with diameters less than or equal to the indicated values. For the prepared alumina powder, the D10, D50, and D90 were 0.384, 0.731, and 2.238  $\mu$ m, respectively (e.g. 10% of particles had a diameter less than or equal to 0.384  $\mu$ m, and so on). The particle size with the highest mass-frequency was 0.596  $\mu$ m. Additionally, an SEM image of the powder taken with secondary electrons is shown in **Figure 7** and is consistent with the particle size and distribution data as well as shows that the particles are relatively spherical (although not perfectly spherical) in shape. For maximum packing efficiency and contact between particles, it is ideal to have particles which are as close to perfectly spherical in shape as possible. These combined data demonstrate that the prepared powder exhibited pure phase and a narrow particle size and distribution centered on a fine particle size. These traits are all desirable for the processing of transparent ceramics in terms of reducing potential scattering sources and improving sinter ability through the high degree of contact between fine particles with high surface areas.

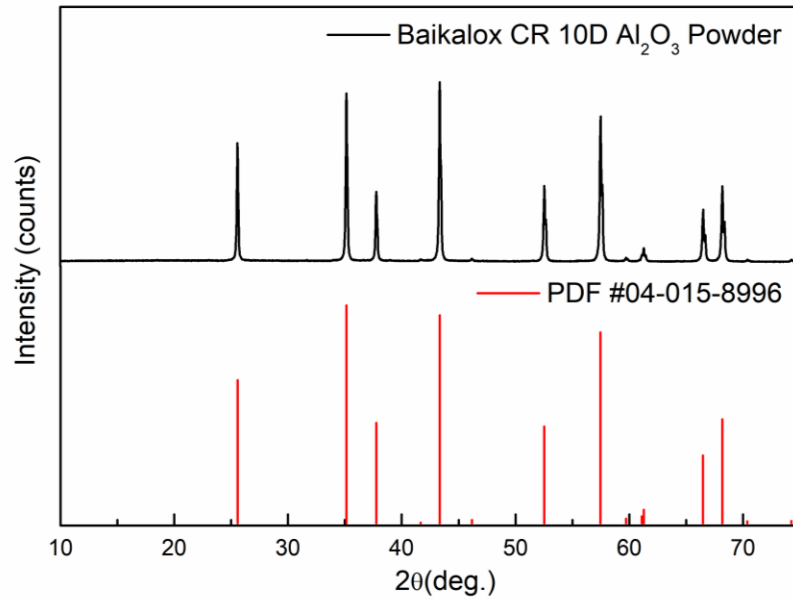


Figure 5. XRD analysis of prepared Al<sub>2</sub>O<sub>3</sub> powder.

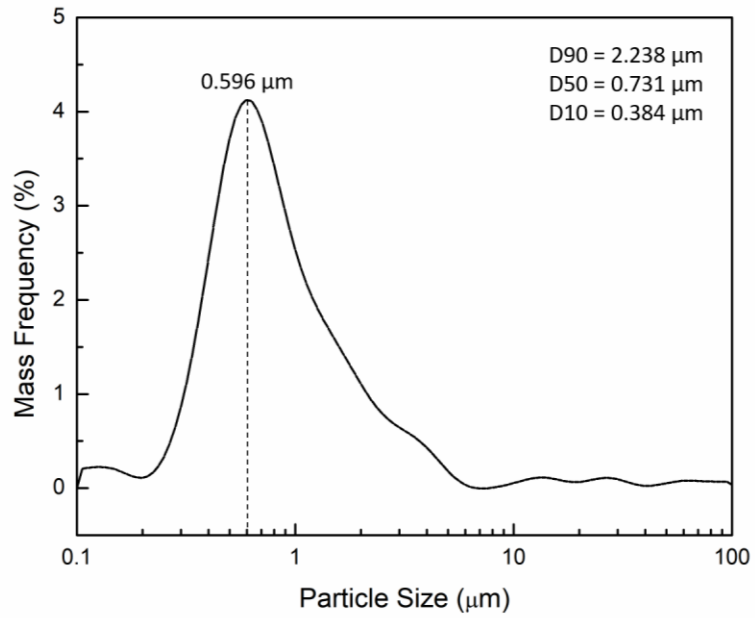


Figure 6. Particle size and distribution of prepared Al<sub>2</sub>O<sub>3</sub> powder.

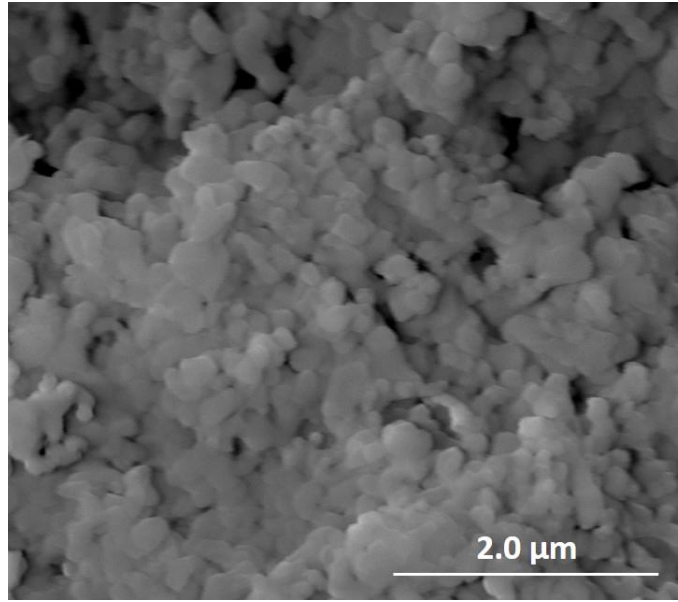


Figure 7. SEM image of prepared Al<sub>2</sub>O<sub>3</sub> powder.

In terms of slurry rheology, the proportions of the batch ingredients were found to significantly affect the viscosity and therefore the behavior of the slurry both qualitatively and quantitatively. The rheology as a function of alumina content is presented in **Figure 8** and the rheology as a function of isobam per mixed powder is presented in **Figure 9** along with the calculated flow index ( $n$ ) values, using Equation 1, in parentheses for the slurries in both figures. The data shows that incremental increases in alumina and isobam per mixed powder as small 2 wt% and 0.3 wt%, respectively, can cause as large as an order of magnitude increase in the viscosity (Pa-s). In practice, higher viscosity slurries tend to exhibit greater control and shape retention than the lower viscosity slurries. On the other hand, the higher viscosity slurries tended to be more difficult to prepare in terms of achieving a homogeneous mixture and thorough de-gassing. Therefore, maintaining a balance between these parameters is necessary for printing. In this case, slurries with 68 – 74 wt% alumina and 0.4 – 1.0 wt% isobam per mixed powder are considered “printable”, with the slurry containing 72 wt% alumina and 0.7 wt% isobam per mixed powder being ideal for printing. Below this range, slurries are not sufficiently viscous for printing and above this range, slurries are too viscous to be properly prepared for printing. Furthermore, it can be seen from both Figure 8 and Figure 9 that all the slurries possessed flow index values less than 1, indicating shear-thinning behavior. Shear-thinning describes a decrease

in viscosity with increasing shear rate, which can also be seen and confirmed by the data.<sup>197</sup> In comparison to other similar works in literature,<sup>195-196</sup> the slurries in this thesis exhibited significantly lower flow index values, indicating very strong shear-thinning behavior. Practically speaking, shear-thinning behavior is necessary for 3D printing with a DIW printer and indicates that there will be a transitional period of rheological behavior before, during, and after extrusion with the 3D printer. Shear-thinning behavior enables a high viscosity slurry to become fluid enough to be extruded through a small nozzle and then return to a higher viscosity state, allowing for proper flow and workability during printing without sacrificing control and final shape retention. Shear-thinning behavior will also be taken into consideration and discussed in subsequent sections of this thesis with regard to 3D printing parameters and achieving a balance between factors such as throughput, printing time, and quality of the printed parts.

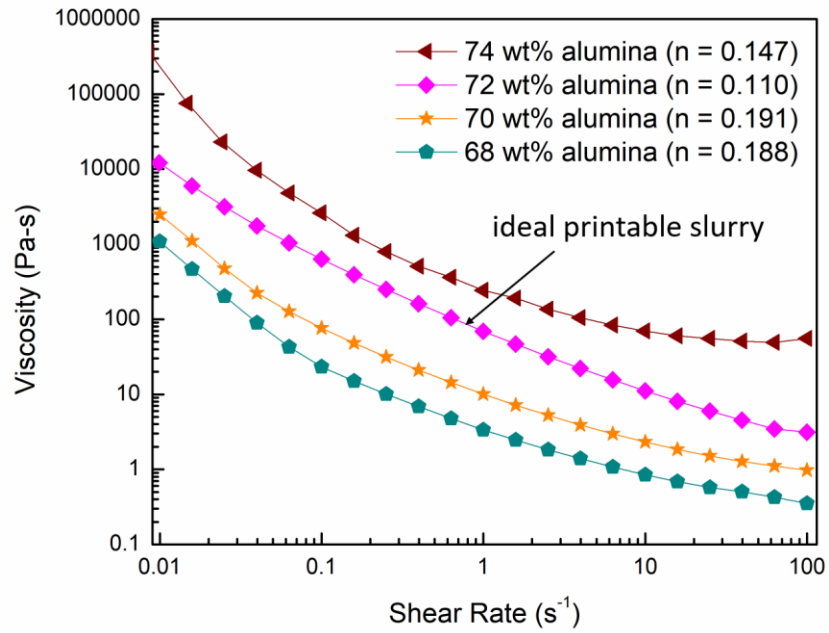


Figure 8. Rheology of slurries with varying alumina content.

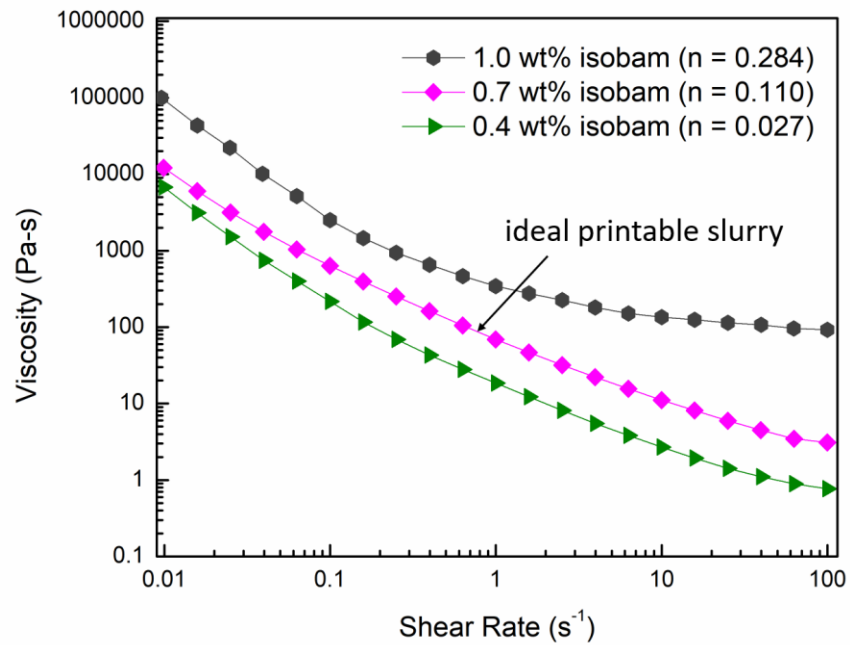


Figure 9. Rheology of slurries with varying isobam per mixed powder.

## D. Conclusions

In summary, this section discusses the starting materials used for 3D printing and how they were used to prepare slurries of suitable behavior for 3D printing. The alumina powder used contained a small fraction of MgO as a sintering aid, but was otherwise of single  $\alpha$ -Al<sub>2</sub>O<sub>3</sub> phase according to the results of XRD analysis. Additionally, the powder was also characterized for SSA and particle size and distribution. It was determined that the particles had a relatively high SSA of  $7.9571 \pm 0.1174$  m<sup>2</sup>/g, were fine in size (50% of the particles less than 0.731  $\mu$ m), and narrowly distributed in size. Furthermore, SEM images show that the particles were not perfectly spherical in shape, yet were relatively spherical. This combined data is desirable for transparent ceramic processing in terms of reducing potential for scattering sources due to impurities as well as indicating good potential densification behavior due to the small particle sizes with high surface areas and nearly spherical shapes for increased packing efficiency and contact between particles.

Using this alumina powder, along with DI water and isobam, multiple slurries were prepared to evaluate rheological behavior both quantitatively and qualitatively. The rheology measurements show that small incremental increases in alumina content and isobam per mixed powder causes significant increases in the viscosity. Higher viscosity slurries are found to exhibit more desirable behavior in terms of potential for 3D printing, but are less process-friendly and consistent than the slurries of lower viscosity. For these reasons, it has been determined that slurries used for 3D printing should contain between 68 – 74 wt% alumina and 0.4 – 1.0 wt% isobam per mixed powder, with an ideal slurry containing 72 wt% alumina and 0.7 wt% isobam per mixed powder. Outside of this range, slurries are either too viscous to prepare properly, or too fluid for printing. Additionally, it has been determined that each slurry exhibited shear-thinning behavior, which is necessary for extruding a viscous slurry through a small nozzle during 3D printing.

### III. 3D PRINTING AND CIP PROCESSING

#### A. Introduction

Conventionally, transparent ceramics have been fabricated using methods such as dry pressing and cold isostatic pressing (CIP), casting, hot-pressing (HP), and others as mentioned previously in Section I part A.<sup>199</sup> These fabrication methods are capable of producing quality transparent ceramics, but are either incapable of fabricating complex structures of varying shapes and sizes or require additional tooling costs and processes to complete such structures. It was not until relatively recent advances in technology occurred that 3D printing has emerged as a viable option for the fabrication of transparent ceramics with the additional benefit of freedom of design. Despite the progress that has been made, 3D printing of quality ceramic structures which possess minimal defects and can be sintered to near-full density requires careful consideration and fine-tuning of the many interconnected parameters in the printing process.

The 3D printer used in this work, the Hyrel System 30M, utilizes a fixed extruder outfitted with different sized nozzles and a computer-controlled build platform which can move in the x-, y-, and z-direction as shown in **Figure 10**. Within the 3D printer's Repetrel software, various part files can be directly uploaded and edited in terms of size and orientation. Furthermore, different printing parameters can be edited within the Slic3r software to change the printing behavior and achieve various outcomes. The most directly applicable 3D printing parameters for the research conducted in this thesis were print move speed, nozzle size, extrusion width, and layer height. Fill density is another important 3D printing parameter and needs to be held at 100% in order to achieve a full density part; for this reason, the fill-density parameter was not experimented with. Print move speed controls the speed of the movements when the extruder is actively building the part. Nozzle size is the inside diameter of the chosen nozzle. Extrusion width is how wide of a path is extruded by the printer and affects how many paths comprise a layer. Layer height is how tall each layer is and therefore how many layers make up a part. The majority of these parameters can be further broken down into subsections for a higher level of control, such as initial layer height, external perimeter print speed, and others. It should be noted that, due to the shear-thinning slurry behavior, 3D printing parameters which effect throughput

will also change the viscosity of the slurry. Since transparent ceramics require near full theoretical density, the parameters must be optimized to achieve a nearly defect free and dense structure. Once each parameter is set, the “print recipe” is saved and “sliced” into G-code (programming language for 3D printers), and the print job is ready to begin. Following printing, it is necessary for the part to dry to complete the forming process.

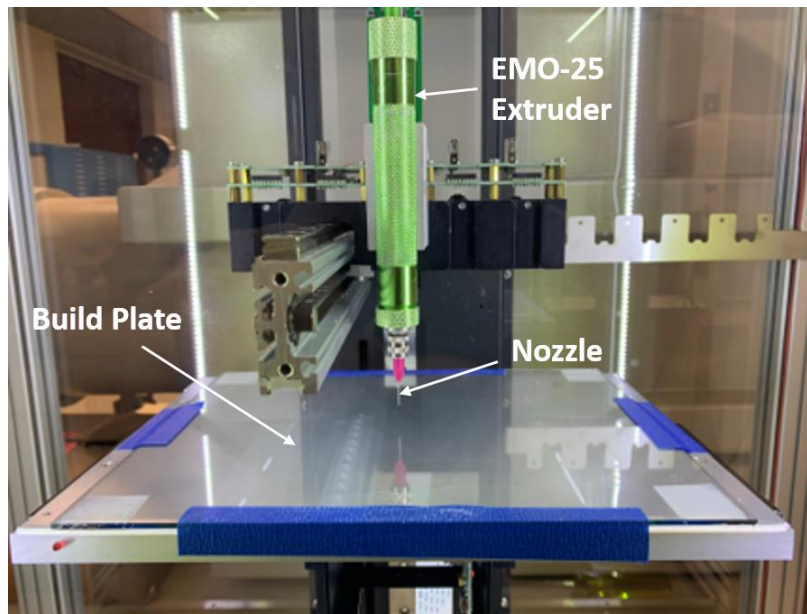


Figure 10. Diagram of Hyrel System 30M 3D printer.

Compared to the 3D printing process, CIP processing is relatively simple. In CIP processing, a dry-press is first used to compact the powder into a disc with the assistance of a binder. Polyvinyl alcohol (PVA) is a commonly used binder for these purposes and was therefore employed for this study.<sup>64-67</sup> The formed disc is then isostatically-pressed by applying pressure via an immersion fluid to compact the disc further and create a relatively dense green body. The dry-pressing and isostatic pressing processes possess few parameters and can only produce limited shapes.

These investigations have been conducted for the fabrication of many samples while optimizing the 3D printing parameters to consistently obtain high quality and dense green ceramic structures of varying shapes and sizes in an efficient manner. Furthermore, the work that has been completed in this section has a direct impact on the results of subsequent post-processing and the final quality of the parts. The 3D printing process and

parameters have been evaluated for printing time, using visual observations during and after printing, and green body density measurements.

## **B. Experimental Procedure**

### **1. 3D Printing**

Different part files were directly uploaded to the Repetrel software in the .stl file format and edited as desired for both orientation and scale in the x-, y-, and z-directions. Printing parameters were selected in the Slic3r software to create a print recipe. Each of the following printing parameters were experimented with to create a wide variety of print recipes: print move speed, nozzle size, layer height, and extrusion width. The following print recipe was used as a “default” from which the previously mentioned parameters were varied from and compared with: print move speed of 1.5 mm/s, nozzle size of 0.84 mm (18-gauge), layer height of 0.4 mm (~47.6% of nozzle size), and extrusion width of 1.26 mm (~150% of nozzle size). Although there were subsections which could be controlled to a higher degree of fidelity, most parameter sets were held constant for a given run. For example, if the print move speed was set to 1.5 mm/s, every print move speed within the run was performed at 1.5 mm/s, rather than making individual adjustments for specific print moves such as external perimeters, infill, and others. Once all the printing parameters were set, the part file was sliced into G-code according to the print recipe using the Slic3r software.

An identical process from Section II part B of this work was used to prepare the “ideal” printable slurry containing 72 wt%  $\text{Al}_2\text{O}_3$  and 0.7 wt% isobam per mixed powder. Following preparation of the slurry, the EMO-25 extruder was loaded with the slurry using a plastic spatula and fitted with the nozzle that corresponded with the printing parameters. The nozzle sizes available with their inside diameters in parentheses were: 16-gauge (1.20 mm), 18-gauge (0.84 mm), 20-gauge (0.60 mm), and 22-gauge (0.41 mm). The extruder was then secured and screwed tightly into the extruder assembly on the 3D printer. Next, a sheet of mylar was taped onto the glass build plate for the part to be built upon. The extruder was calibrated to the build plate with the mylar on it using the z-calibrate feature and a piece of paper placed on top of the build plate and mylar by raising the build platform until the nozzle barely contacted the paper. Once calibrated, the extruder was primed until

there was a consistent flow of material, after which the print job was started and the calculated time to print provided by the software was recorded.

During printing, observations were recorded to evaluate slurry performance, adhesion and formation of layers, infill characteristics, dimensional accuracy, and visual quality. Small adjustments were made mid-print using the “z-fine adjustment” tool which moves the build platform vertically by 25  $\mu\text{m}$  to maintain a proper distance between the nozzle and build platform or part as needed. Following a successful print, the mylar sheet with the part built upon it was removed from the build plate and set aside for visual inspection prior to being covered for drying at room temperature for 24 hours. This process was repeated for all printed parts. After 24 hours of drying, the parts which were of acceptable quality were kept for additional processing. Furthermore, the green body density was recorded of numerous parts that could be determined from physical measurements using a caliper and mass balance. The green body density was reported as a percentage relative to the theoretic density of  $\alpha\text{-Al}_2\text{O}_3$  reported to be  $3.98 \text{ g/cm}^3$  within the ICDD database as matched from the previous XRD analysis in Section II part C. It should be noted that more precise density measurements, such as the Archimedes method, could not be used since an immersion fluid would destroy the green body.

## **2. CIP Processing**

The powder was prepared for dry-pressing by combining approximately 2 g of alumina powder with 0.25 mL of Sigma-Aldrich 98-99% hydrolyzed PVA (molecular weight 31,000- 50,000) and thoroughly grinding and mixing the two with a mortar and pestle until homogenized. The mixture was then loaded into a circular die of approximately 2 cm in diameter and dry-pressed using a Carver, Inc. manual uniaxial press with a force of 1 metric-ton for 5 seconds. The resulting pressed disc was wrapped using pieces of a nitrile glove and placed within a flexible plastic pouch. The plastic pouch was vacuum sealed and loaded into an Autoclave Engineers CP 360 Cold Isostatic Press. The CIP process was performed at a pressure of 250 MPa for 1 minute. Following CIP, the disc was removed and measured for its volume and mass to calculate the green body density. This process was repeated to produce many nearly identical samples.

## C. Results and Discussion

### 1. 3D Printed Samples

Various ceramic parts were successfully fabricated via 3D printing using the Hyrel System 30M, EMO-25 extruder, a variety of print recipes, and printable slurries. Representative images of the fabricated ceramics are shown in **Figure 11**. These images demonstrate the capacity of 3D printing to fabricate many different parts which vary in both complexity of shape as well as size utilizing the same materials, equipment, and processes. Printing parameters were observed to significantly affect the efficiency of the printing process, throughput and slurry behavior (due to shear-thinning), and quality of the output part. Although many printing defects are inherent to the 3D printing process, such as inconsistent printing of paths/layers, formation of “blobs”, insufficient initial and interlayer adhesion, and others, experimenting with and optimizing the printing parameters made it possible to mitigate or even remove some defects. If a part possessed printing defects which were deemed too significant to be usable, however, the part was not carried through the remainder of the process. The average relative green body density across the measured 3D printed parts was  $1.68 \pm 0.05 \text{ g/cm}^3$ .

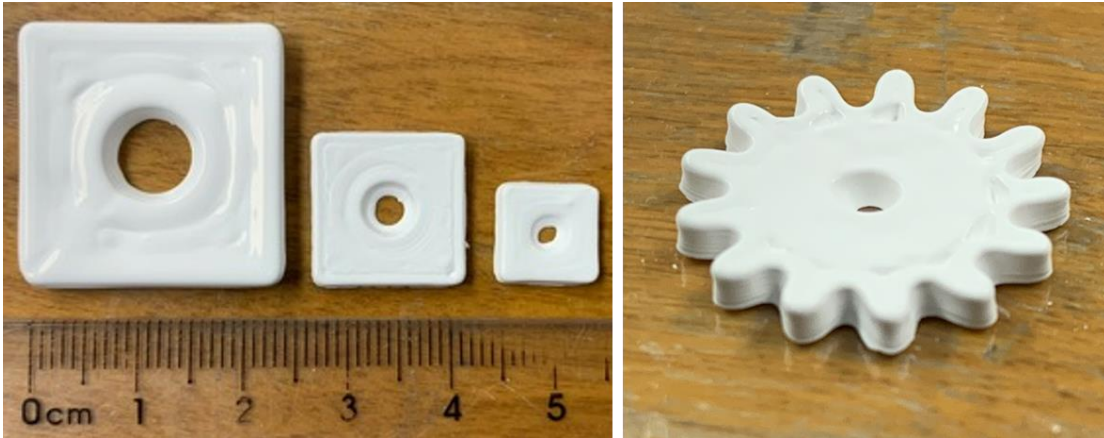


Figure 11. 3D printed alumina ceramics.

### a. Print Move Speed

The print move speed was found to have a significant effect on the continuity of the print as well as initial and interlayer adhesion. When the print move speed was set to 5 mm/s or higher, the build platform was moving too fast for the slurry to handle. This mismatch resulted in improper adhesion and print lines became inconsistent or broken. In other words, the slurry was unable to sufficiently flow out of the extruder and form onto the surface (build plate or previous layer) causing the extruded slurry to tend to be pulled into a line which was thinner than expected and would often break. This problem was mitigated by decreasing the print move speed. However, when the print move speed was set to 1 mm/s or slower, the print time became excessively long. The slow print speed and long print time would cause additional problems such as print lines and layers drying mid-print and the nozzle becoming clogged due to the low throughput. Therefore, a print move speed between 1.5 – 4.0 mm/s was slow enough to enable proper adhesion and forming, yet fast enough to prevent premature drying and clogging of the nozzle. **Figure 12** shows the print time (calculated by the Repetrel software) as a function of print move speed for a rectangular prism part of 15 mm x 15 mm x 3 mm printed under the default parameters. It can be seen that small changes in the print move speed, such as 1 mm/s, can affect the print time of the parts in this study significantly. Within the 1.5 – 4.0 mm/s range, there was no significant difference observed in the quality/properties of the printed parts.

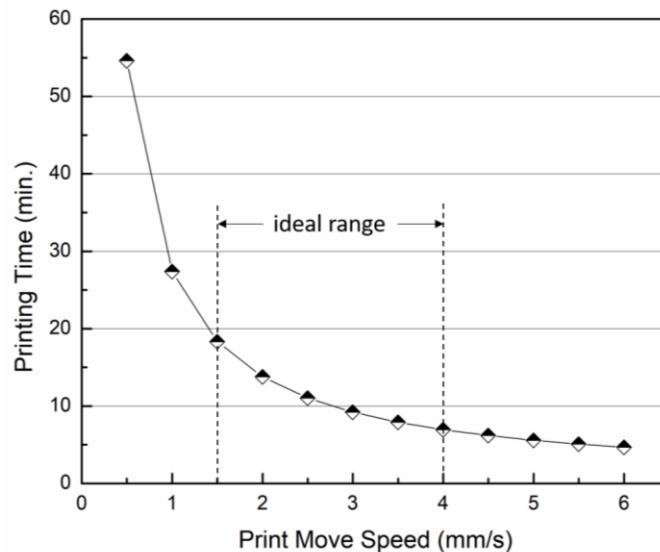


Figure 12. Printing time as a function of print move speed.

### b. Nozzle Size, Layer Height, and Extrusion Width

The nozzle size, layer height, and extrusion width are all somewhat interconnected and are typically expressed as percentages of one another. It was crucial to fine-tune these parameters to achieve good quality parts. In general, smaller values of these parameters results in improved quality and accuracy of the printed parts at the cost of longer printing times/lower throughput. However, as with the previous parameters, it was determined that is necessary to find a well-balanced set of values for each to achieve the best quality parts.

Depending upon the size of the part, certain nozzle sizes are more appropriate. For example, if a relatively large nozzle size is chosen for a small part with fine details, the nozzle will be inherently incapable of producing it well. On the other hand, if a small nozzle is chosen for a large part, the part will take excessively long to print, causing issues with premature drying and adhesion between layers. **Figure 13** presents the printing time (calculated using the Repetrel software) as a function of nozzle size for the same 15 mm x 15 mm x 3 mm rectangular prism part printed under the default parameters. It can be seen that as the nozzle size decreases, there is a significant increase in printing time. As a general guideline and recommendation based on observations, the nozzle size should not exceed about 20% of the smallest feature size nor be smaller than about 4% of the longest dimension of the structure to maximize both quality and efficiency.

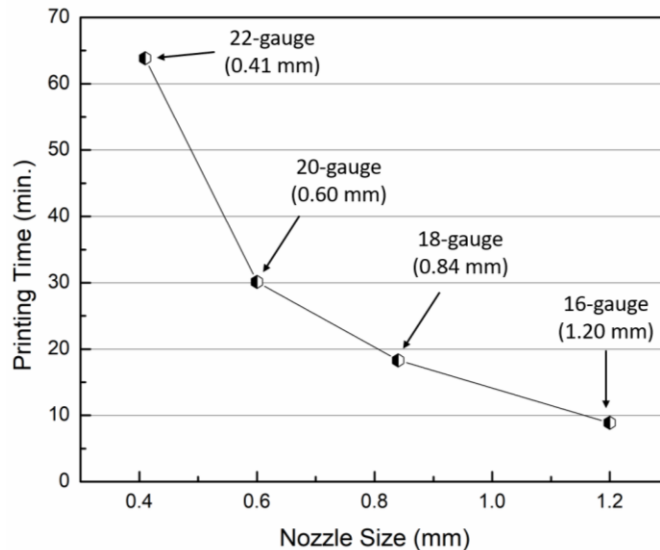


Figure 13. Printing time as a function of nozzle size.

For layer height, it has been determined that a value between approximately 25 – 70% of the nozzle diameter is suitable for printing. When the layer height is larger than 70%, despite the print time being fast, there is an excessively high throughput which leads to poor control and low dimensional accuracy. However, when the layer height was less than 25% of the nozzle size, the layers were too thin and the print time was too long, resulting in pre-mature drying and poor interlayer adhesion/formation. In between this range, adequate parts could be produced. **Figure 14** shows the calculated printing time as a function of layer height for the same aforementioned rectangular prism part being printed with a 0.84 mm nozzle. It can be seen that as the layer height increases, the printing time decreases, until around 0.4 mm (~48% of nozzle size), after which there is not a significant decrease in printing time. This indicates that there is no significant additional benefit in increasing the layer height past this point, making a value of ~48% of the nozzle size an ideal balance between quality and time efficiency. It was also found that the layer height does more than effect the part visually. When five identical parts were all printed under the default parameters but with different layer heights, there was a measurable difference in their green densities. **Figure 15** shows the relative green density of the five parts as a function of their layer height along with inset images of the green parts with 0.3 mm and 0.5 mm layer heights as an example for visual comparison. It can be seen that as the layer height increases, the relative green density decreases. This is likely due to two observable tendencies. First, parts with small layer heights tend to have smaller defects that are “corrected for” or “covered up” by the many layers which are printed on top of it as opposed to parts with large layer heights which typically have larger defects and fewer subsequent layers to fix the problem. Second, parts with large layer heights tend to form more loosely packed edges and layers as opposed to the small layer height parts which form more densely packed layers and edges as supported by the inset photographs shown in Figure 15.

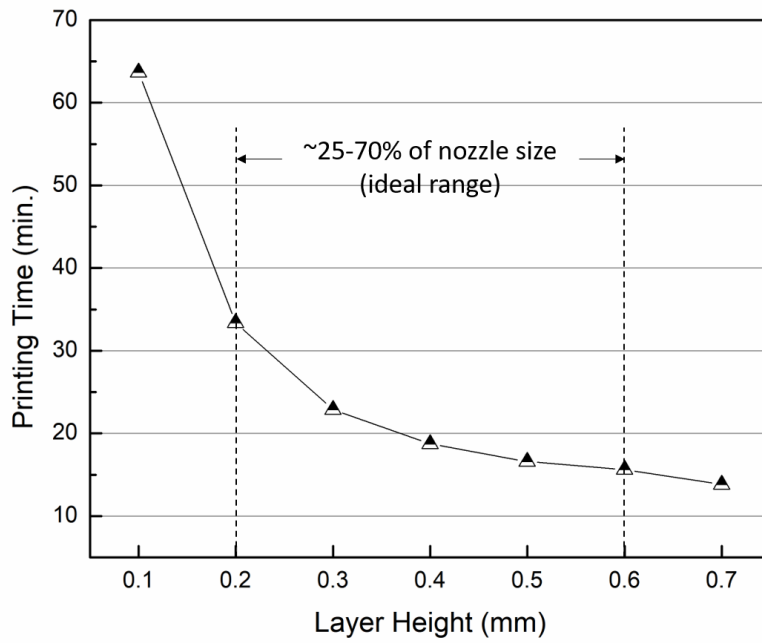


Figure 14. Printing time as a function of layer height.

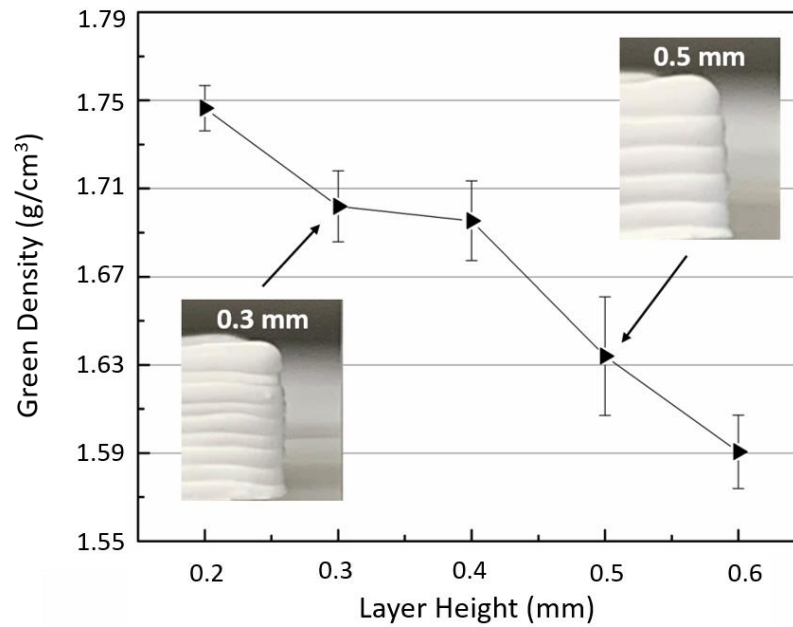


Figure 15. Green density as a function of layer height.

For extrusion width, the parameter needs to be just large enough to sufficiently infill the part and create a dense green body. A value of approximately 150% of the nozzle size is sufficient for creating an overlap between each printing path, thus ensuring complete infill without noticeable changes in surface/edge finish or dimensional accuracy. **Figure 16** shows the results of using vastly different extrusion width values to clearly demonstrate its effect. When the extrusion width is too small, there are gaps in the structure (insufficient infill/under-extrusion), and when the extrusion width is too large, there is a loss in accuracy and fine finish on the surface/edge (over-extrusion). When the parameters are set properly, however, it can be seen that a filled-in structure with a fine finish along the surface and edges is achieved.

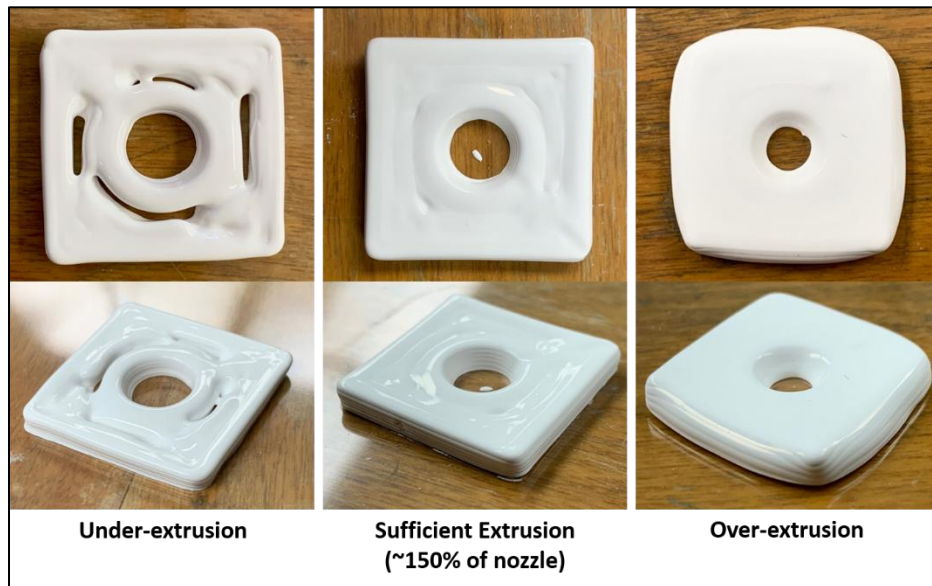


Figure 16. Alumina ceramics 3D printed with varying extrusion widths.

## 2. CIP Samples

The CIP process does not possess many variables to fine-tune and the parts produced were of sufficient quality under the set processing parameters. An example picture of a CIP processed sample is shown in **Figure 17**. It can be seen that the part is of a simple disk-shape and does not possess any significant defects. The average relative green body density of the CIP samples was  $1.71 \pm 0.04 \text{ g/cm}^3$ . This density value is higher and has a smaller standard deviation than the 3D printed samples, indicating that CIP processing can produce denser and more consistent green bodies. A possible explanation for this is the combination of a lack of significant inherent defects introduced in the dry-pressing process as well as the subsequent CIP process enables a higher formed density through additional compaction.

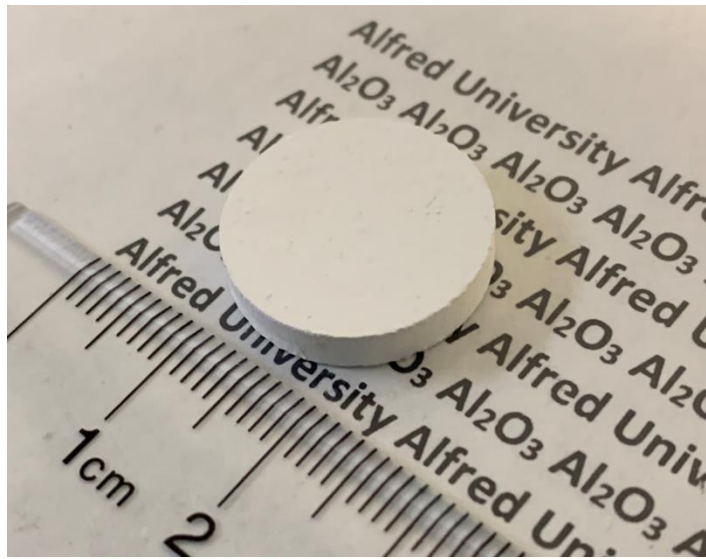


Figure 17. CIP processed alumina ceramic.

## **D. Conclusions**

In this section, it has been demonstrated that 3D printing can produce alumina ceramic samples of varying shapes/sizes without making significant changes to the materials and processes. Furthermore, quality printed parts and efficient processing can be achieved through the optimization of printing parameters such as: print move speed, nozzle size, layer height, and extrusion width. Additionally, CIP alumina samples of nearly identical disk-shapes were fabricated as a conventional forming method to compare to. The CIP samples achieved slightly higher green body densities and less variability in the density values than the 3D printed samples, which is likely due to inherent defects introduced through 3D printing that are not experienced in dry-pressing as well as the additional compaction of the body through the subsequent CIP process.

# **IV. POST-PROCESSING**

## **A. Introduction**

Following fabrication of a ceramic part, post-processing steps are critical to maintaining the quality established in the green bodies and achieving the desired final properties. Drying and debinding processes involve heating the ceramic to a temperature at which the water and organic content is fully removed to prepare the green body for sintering. Vacuum sintering processes are then used to densify the green body. Lastly, polishing is performed to reduce the surface roughness. In these processes, it is important to handle the samples carefully and use slow heating rates to avoid cracking.

As mentioned previously, transparent ceramics are able to achieve the greatest optical quality when they simultaneously possess high density, minimal defects and secondary phases, low surface roughness, and small grain sizes. Traditionally, single-step sintering (SSS) profiles are used to densify ceramics, through simply heating the ceramic from room temperature to a chosen temperature, holding at that temperature for a chosen time, and cooling down to room temperature. It is well-known, and has been widely demonstrated, that as sintering temperature and sintering time increase, the density and grain size will increase as well. This means that at the high temperatures required for full-densification, significant grain growth will also be present. For optical ceramics, it is

important to have small grain sizes to reduce scattering. Furthermore, from an application stand point, large grain sizes are also undesirable in achieving good mechanical properties.<sup>200-202</sup> As an alternative, two-step sintering (TSS) profiles offer a potential improvement for transparent ceramic processing. Using a TSS profile, the ceramic is heated from room temperature to the sintering temperature and then immediately dropped to a lower temperature where it is held for a chosen time before cooling back down to room temperature. For a TSS profile, the high starting temperature initiates grain boundary diffusion, while the lower holding temperature limits grain boundary migration, thus enabling the suppression of grain growth during densification.<sup>203-205</sup>

In this section, the drying, debinding, sintering, and polishing parameters are studied for the 3D printed and CIP processed ceramics. These investigations include using both SSS and TSS profiles. The goal of this study has been to establish a set of parameters which is capable of achieving high-quality transparent ceramics as well as determine the merit of 3D printing as a method of transparent ceramic fabrication when compared to more conventional methods. The fabricated ceramics have been evaluated for their quality and transparency using their phase purity, density, average grain size, and total transmittance as well as their visual appearance.

## **B. Experimental Procedure**

The previously prepared 3D printed and CIP samples, as described in Section III, were transferred to a Quincy Lab, Inc. Model 30 GC Lab Oven held at approximately 70°C and dried for 24 hours. The oven dried samples were then debinded in a Neytech Vulcan Benchtop Furnace Model 3-550 under the following profile: heat from room temperature to 500°C at a rate of 0.5°C/min, hold at 500°C for 4 hours, heat from 500°C to 1000°C at a rate of 1°C/min, hold at 1000°C for 3 hours, auto-cool to room temperature. The debinded samples were placed into a Thermal Technology Inc. High Vacuum Graphite Furnace to sinter using either an SSS or TSS profile. The SSS profile was as follows with the final sintering temperature ranging from 1650 – 1875°C: heat from room temperature to 1300°C at a rate of 10°C/min, hold at 1300°C for 1 hour, heat from 1300°C to the final sintering temperature at a rate of 2°C/min, hold at the final temperature for 6 hours, and cool to room temperature at a rate of 10°C/min. Alternatively, the TSS profile was as follows: heat from

room temperature to 1300°C at a rate of 10°C/min, hold at 1300°C for 1 hour, heat from 1300°C to either 1850°C or 1875°C at a rate of 2°C/min, cool to 1800°C at a rate of 2°C/min, hold at 1800°C for 8 hours, and cool to room temperature at a rate of 10°C/min.

Following sintering, XRD measurements were conducted using a Bruker D2 Phaser and Cu k-alpha radiation (30 kV, 10 mA) with a start and end angle of 10° and 75° 2 $\Theta$ , respectively, step size of 0.02° 2 $\Theta$ , and count time of 0.3 s. The XRD data were analyzed using MDI Jade 9 and PDF-4+ software as well as the ICDD database for phase identification. Density measurements were conducted using the Archimedes method at room temperature with DI H<sub>2</sub>O as the immersion liquid. The sintered samples which were visibly transparent were grinded down to a flat surface with a thickness of approximately 1.5 mm and polished using a Buehler EcoMet 3000 Variable Speed Grinder-Polisher and a MetLab Corporation 6  $\mu$ m diamond suspension. Total transmittance measurements were conducted on the polished sample using a Thermo Scientific Evolution 220 UV-Visible Spectrophotometer in the wavelength range from 190-1100 nm. Any opaque, translucent, or poorly transparent samples were not grinded or measured for total transmittance but still received polishing for microstructure evaluation. The polished samples were thermally-etched using the following profile to expose the grain boundaries: heat from room temperature to 1450°C at a rate of 5°C/min, hold at 1450°C for 5 hours, cool to room temperature at a rate of 10°C/min. The microstructure was documented by first gold-coating the sample using a Cressington Sputter Coater 108 and then viewing and capturing images of the sample on an FEI Quanta 200F Scanning electron microscope using a combination of both secondary and backscattered electrons. The average grain size was measured using the line-intercept method and Nano Measurer 1.2 software.

### C. Results and Discussion

Transparent alumina ceramics have been successfully fabricated via 3D printing and post-processing steps including debinding, vacuum sintering, and polishing. **Figure 18** shows examples of transparent ceramic samples formed via 3D printing. **Figure 19** presents photographs of a representative sample through each step of the process. Combined, Figures 18 and 19 demonstrate the progression through the process and transparency of samples visually. When the sintered samples were analyzed via XRD, it

was determined that the diffraction pattern matches PDF #04-015-8996 ( $\alpha$ - $\text{Al}_2\text{O}_3$ ) as shown in **Figure 20**. As compared with the diffraction patterns from the PDF card (lower), prepared alumina powder from Section II (center), and a representative sintered alumina ceramic (upper), it can be seen that the patterns match nearly perfectly with no other phases detected. The XRD results and analysis indicate that no additional impurities or secondary phases were accumulated due to the 3D printing and post-processing. The slight variations in the relative intensities of the peaks among the three diffraction patterns could be due to differences in the orientation and size of crystallites in a powder as opposed to a formed/sintered sample. The properties of the fabricated ceramics such as density, grain size, and transmittance were found to be highly dependent on the sintering conditions. Sintering parameters were varied in terms of both holding temperature and holding time. Furthermore, single-step sintering (SSS) and two-step sintering (TSS) profiles were investigated.

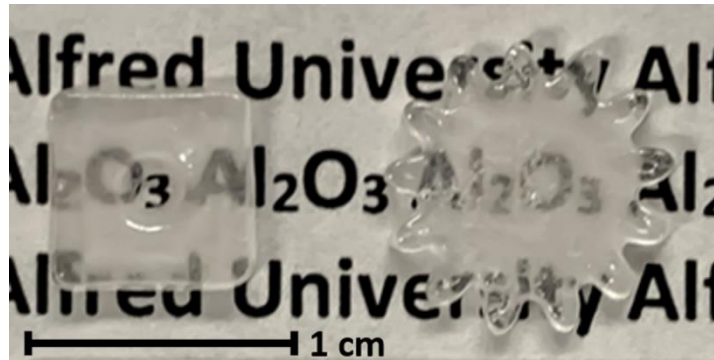


Figure 18. 3D printed transparent alumina ceramics.

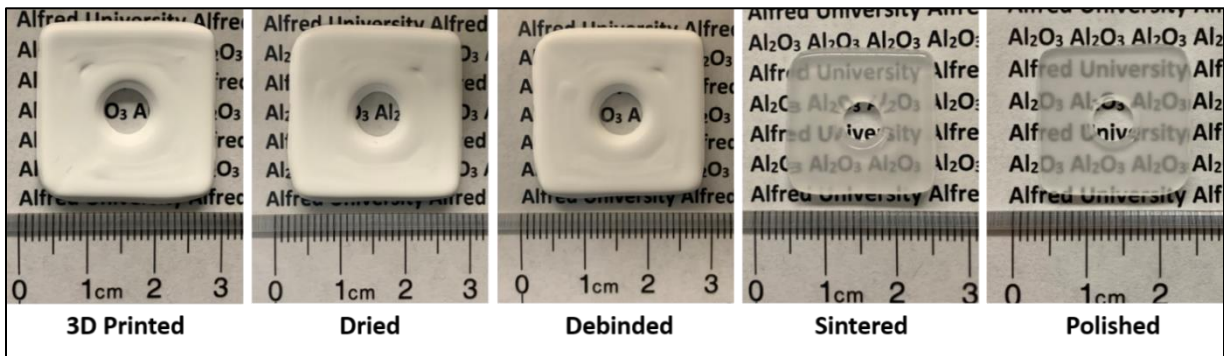


Figure 19. Progression of a representative sample through the process.

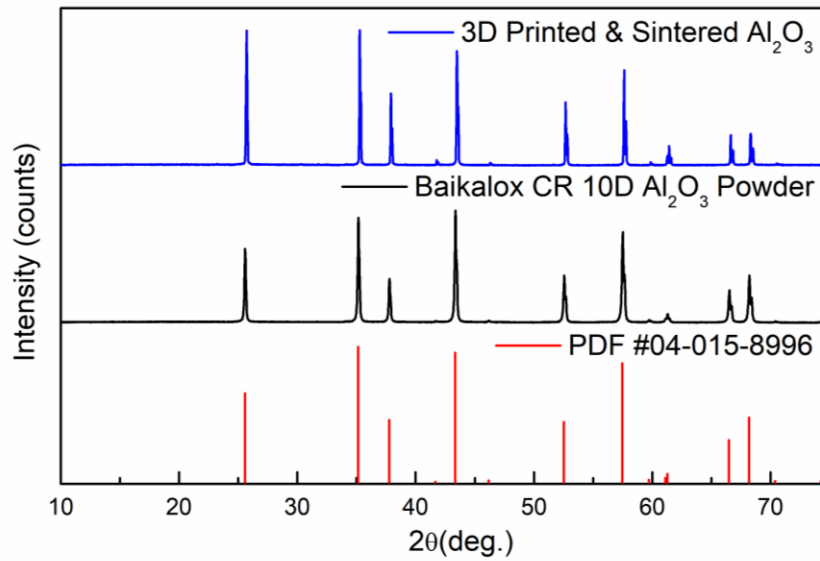


Figure 20. XRD analysis of sintered alumina ceramics.

**Figure 21** presents the relative density as a function of sintering temperature for 3D printed samples sintered using SSS profiles with a hold time of 6 hours and TSS profiles along with data from CIP samples to compare with. Among all samples, it can be seen that the density increases significantly with sintering temperature and reaches near-full density values at the highest tested temperature of 1875°C. Furthermore, it can be seen that all the samples achieved nearly identical density values at this peak point, with the CIP TSS samples achieving only slightly higher densities than the rest. The peak density values achieved by 3D printing were  $99.91 \pm 0.08\%$  for SSS and  $99.92 \pm 0.03\%$  for TSS while the highest CIP density achieved was  $99.93 \pm 0.05\%$  using a TSS profile. Additionally, the relative density as a function of sintering time for the 3D printed samples sintered using SSS profiles at a holding temperature of 1850°C is presented in **Figure 22** along with data from CIP samples to compare with. This data demonstrates that the ceramic does not reach the highest density attainable until 4 hours of sintering, after which the density remains relatively constant. Furthermore, even when sintered under identical profiles, the CIP samples achieved higher densities. Referring back to Section III Part C, the CIP samples were able to achieve higher green body densities due to fewer processing defects and additional compaction during forming. The lower green body density of the 3D printed

samples limits the density which can be achieved through sintering, which is an explanation for why the CIP samples were denser after sintering even under identical profiles. Additionally, also in Section III Part C, the 3D printed ceramics show an increase in green density with decreasing layer height. When these same samples with varying layer heights were sintered using identical SSS profiles at 1850°C for 6 hours, the trend of increasing density with decreasing layer height was observed again, as shown in **Figure 23**. This information further supports the claims/results from earlier where it was noted that parts with large layer heights tend to have larger defects and fewer densely-packed layers and edges than parts with smaller layer heights.

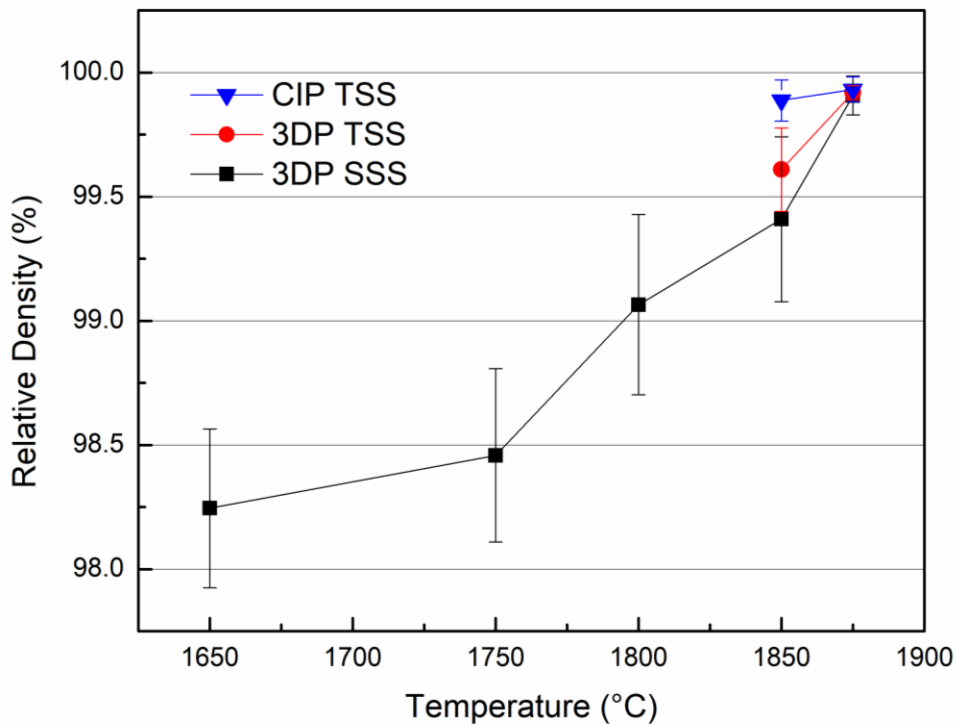


Figure 21. Relative density as a function of sintering temperature for 6-hour hold time.

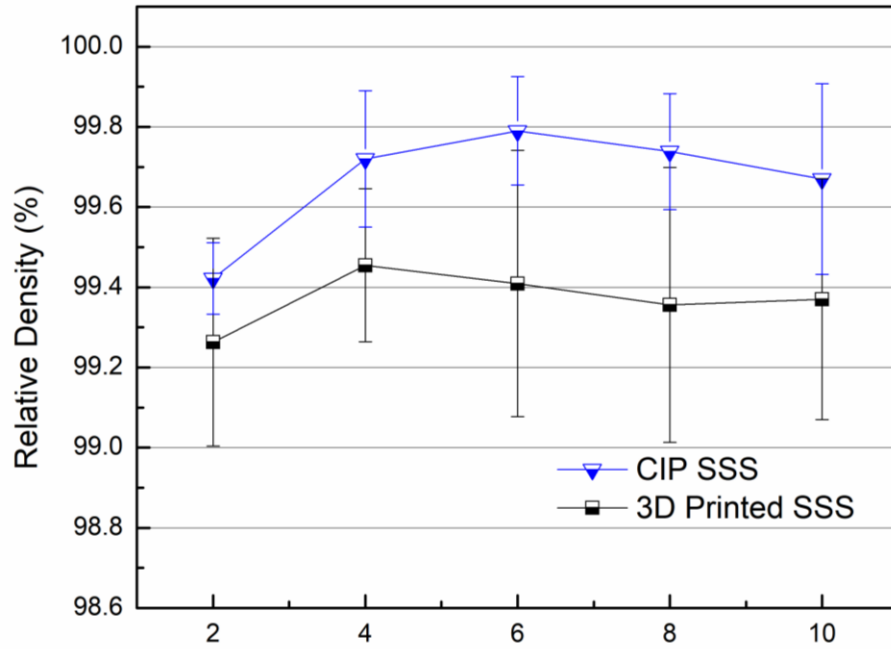


Figure 22. Relative density as a function of sintering time at 1850°C.

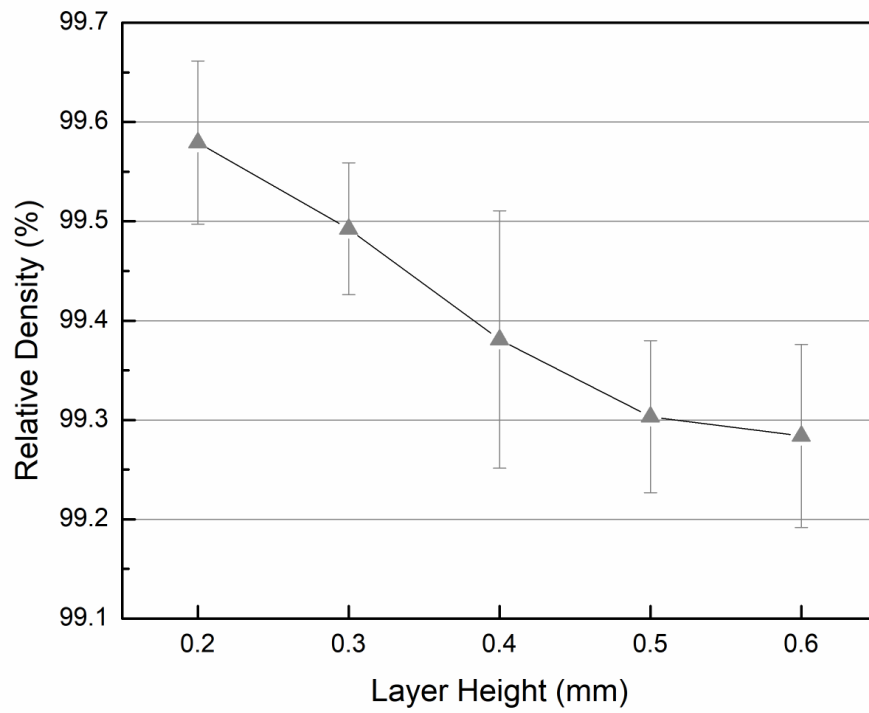


Figure 23. Relative sintered density at 1850°C for 6 hours as a function of layer height.

The average grain size as a function of sintering time for 3D printed samples sintered using an SSS profile at 1850°C is presented in **Figure 24** along with representative images of the microstructure from SEM in **Figure 25**. These data show that both the average grain size and variation in grain size increases significantly with sintering time. Furthermore, the SEM images demonstrate this grain size-sintering time trend visually as well as show that the microstructure is dense and free of significant pores and secondary phases. Additionally, the average grain size as a function of sintering temperature for 3D printed samples for both SSS and TSS profiles is presented in **Figure 26** along with the representative images of the microstructure from SEM for the SSS and TSS samples in **Figure 27** and **Figure 28**, respectively. In a similar trend, the average grain size and variation in grain size increases significantly with sintering temperature. Furthermore, it is demonstrated that TSS profiles can lead to a reduction in grain size at identical sintering temperatures. For example, at 1875°C, the SSS samples have an average grain size of  $113.27 \pm 17.48 \mu\text{m}$  while the TSS samples have an average grain size of  $87.69 \pm 13.53 \mu\text{m}$ . Again, the SEM images also demonstrate the grain size-sintering temperature trend visually and show a dense microstructure free of pores and additional phases. These data, combined with the previous density data, show that TSS profiles can help to achieve full-density while limiting grain growth, which is beneficial for transparent ceramic processing.

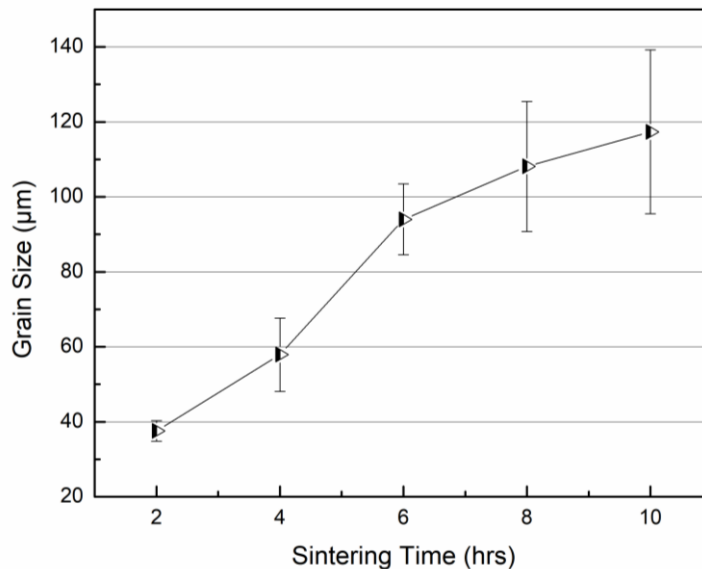


Figure 24. Average grain size as a function of SSS time at 1850°C.

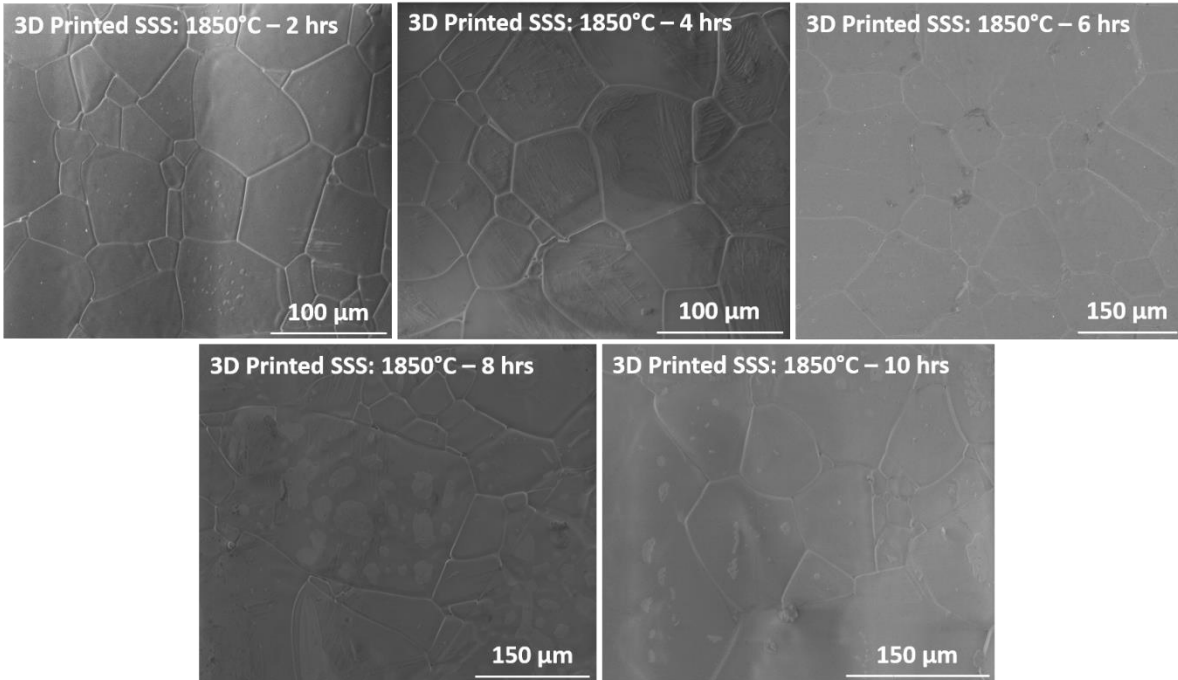


Figure 25. SEM microstructure images of SSS ceramics at 1850°C for varying times.

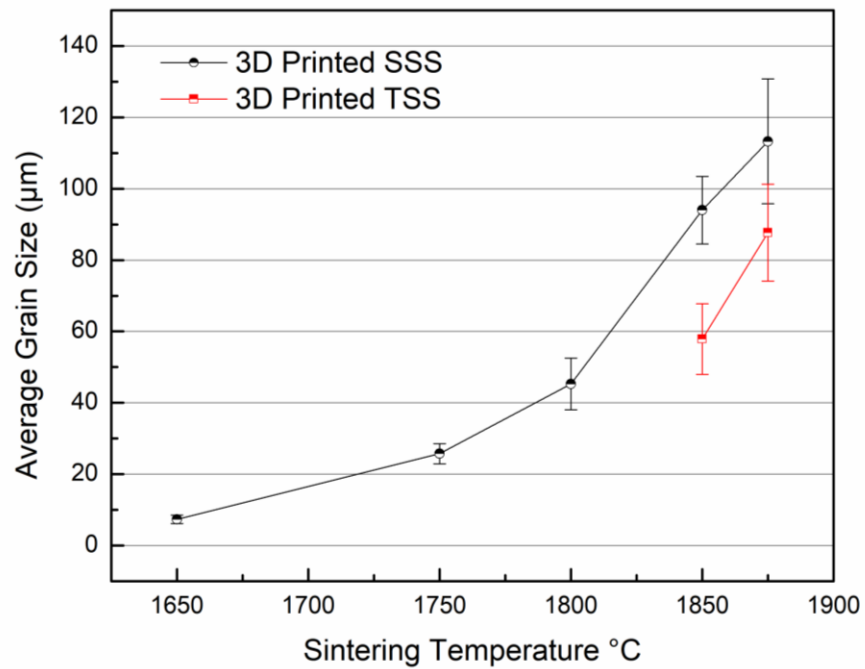


Figure 26. Average grain size as a function of sintering temperature for SSS and TSS ceramics.

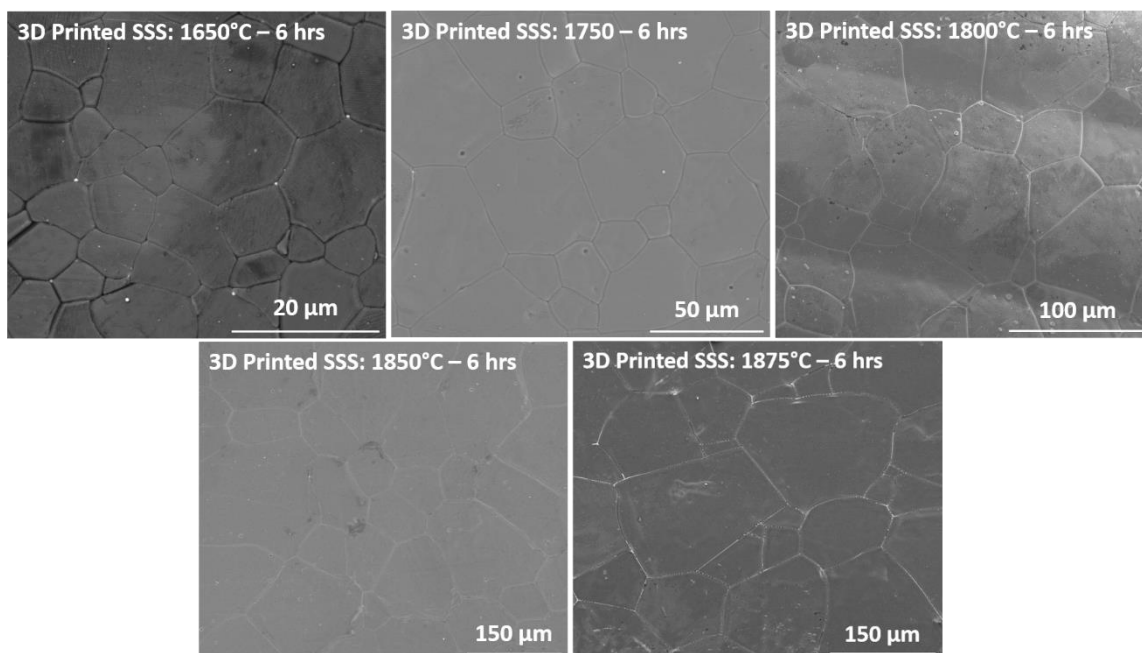


Figure 27. SEM microstructure images of SSS ceramics sintered at varying temperatures for 6 hours.

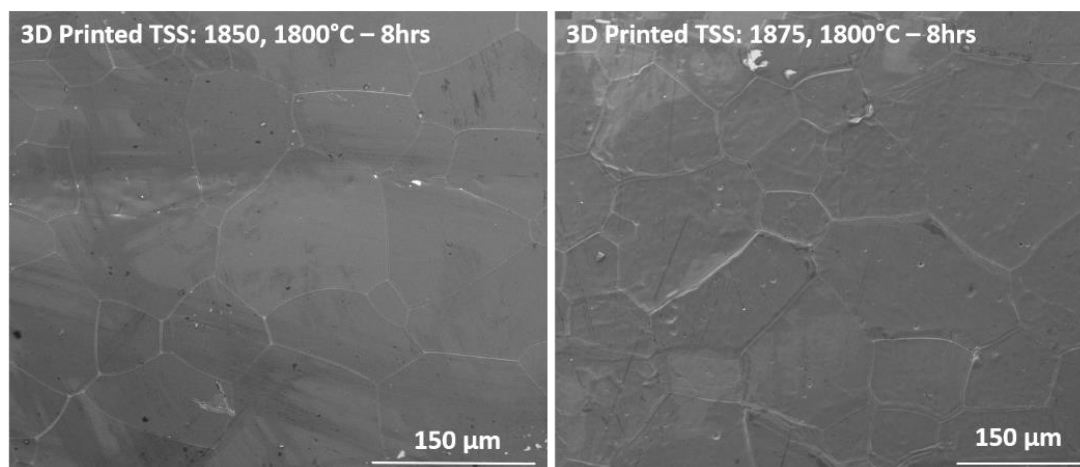


Figure 28. SEM microstructure images of TSS ceramics sintered at varying temperatures.

The most visually transparent of the sintered ceramics were grinded and polished down to an approximately 1.5 mm thickness and measured for total transmittance. Samples which were sintered below 1850°C were found to be either opaque or only somewhat translucent, so they were not measured for total transmittance. **Figure 29** presents the measured total transmittance data along with inset photographs of some of the best samples between SSS and TSS as well as 3D printing and CIP processing. It can be seen from both the data and the photographs that the best 3D printed and CIP processed ceramics achieved similar levels of transparency. The total transmittance measurements show that the 3D printed and CIP processed TSS ceramics reached nearly identical maximum values of approximately 70% at wavelengths above 800 nm (near IR range). In the visible wavelength range (~400 - 700 nm), however, there was a more significant measurable difference between the samples. For example, at 400 nm, the CIP TSS sample reached about 65% transmission while the 3D printed TSS samples reached only about 61% and 59% at 1875°C and 1850°C, respectively. This slight drop-off in transparency from CIP to 3D printing is likely due to defects introduced in the printing process causing scattering as well as limiting the density which can be achieved through sintering. The 3D printed SSS samples were significantly less transparent than the rest and reached at most approximately 63% transmission at 800 nm and above and even lower in the visible range when sintered at 1850°C. The reason for lower transmission is because the SSS samples have both lower densities and larger grain sizes than the other samples. These results demonstrate that 3D printed ceramics can achieve similar optical properties to CIP processed ceramics and that TSS profiles can yield improved transparency over SSS profiles.

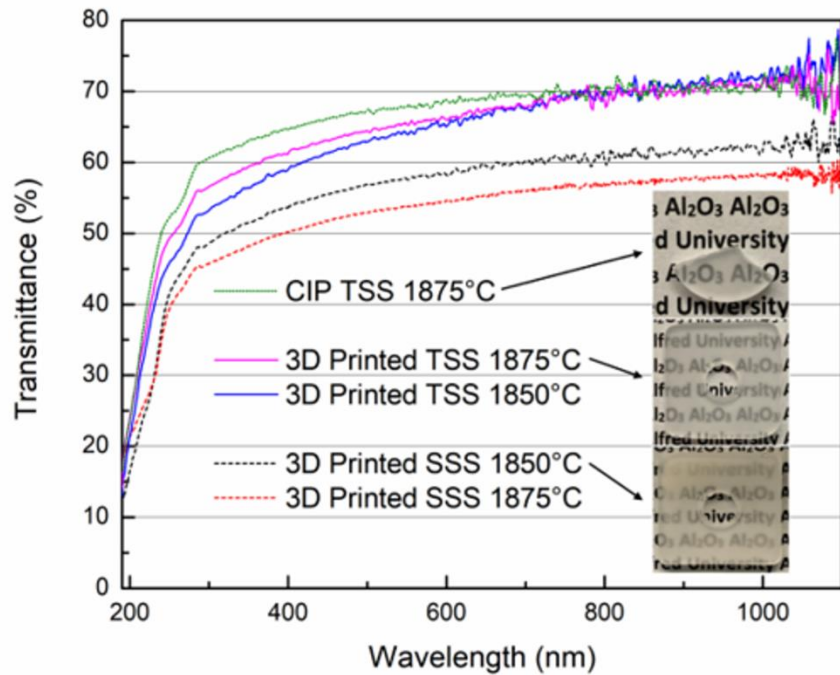


Figure 29. Total transmittance measurements for alumina ceramics from 3D printing and CIP.

In comparison to the results of other works in literature which used conventional processing methods, the 3D printed samples in this report achieve similar results. Kim et al. reported on SPS processed alumina ceramics of 1 mm thickness which achieved a maximum total transmittance of approximately 80% above 1000 nm, but about 70% at 800 nm.<sup>206</sup> Yang et al. also reported on 1 mm thick transparent alumina ceramics fabricated by isostatic pressing and sintering in H<sub>2</sub> atmosphere which achieved a total transmittance as high as 86% between about 300 – 800 nm.<sup>207</sup> These values from literature are higher than what was achieved in this report, which can be attributed to the significant difference in thickness between the samples (1 mm vs 1.5 mm), since transmittance decreases with increasing sample thickness. When taking into account the difference in thickness, though, the results become more comparable.

## **D. Conclusions**

The data in this section indicates a few major conclusions for this work. First, transparent ceramics of varying shapes and sizes can be made successfully through 3D printing and post-processing steps including debinding, vacuum sintering, and polishing. Furthermore, the sintering parameters, such as sintering temperature, hold time, and use of SSS and TSS profiles, significantly affect the density, grain size, and total transmittance of the fabricated ceramics. When the sintering parameters are optimized, it is possible to achieve density and total transmittance values through 3D printing which are similar to those of more conventional CIP processed structures. The best 3D printed sample was achieved through a TSS profile up to 1875°C and then held at 1800°C for 8 hours. This sample reached  $99.92 \pm 0.03\%$  relative density, an average grain size of  $87.69 \pm 13.53 \mu\text{m}$ , and total transmittance values of about 70% above 800 nm and about 61% at 400 nm. In comparison, a CIP sample sintered using the same profile achieved  $99.93 \pm 0.05\%$  relative density and total transmittance values of about 70% above 800 nm and about 65% at 400 nm.

## **V. SUMMARY AND CONCLUSIONS**

Using an extrusion-based 3D printer and post-processing steps, including debinding, vacuum sintering, and polishing, it has been demonstrated that near full-density transparent alumina ceramics of varying shapes and sizes can be fabricated which are of optical quality comparable to that achieved using more conventional processing methods for transparent ceramics, such as CIP. The best quality 3D printed transparent ceramics have been achieved through the use of optimized slurry and printing process parameters as well as a two-step sintering profile. With conventional methods, fabricating transparent ceramics of varying shapes and sizes would require additional tooling costs and processes. In this study, the same 3D printer and process have been used throughout, with only slight adjustments made to specific parameters. Furthermore, the simplistic nature of the extrusion-based 3D printer, as compared to other 3D printing methods, along with the aqueous slurry and use of a vacuum furnace, allows for relatively conventional ceramic processing principles and know-how to be applied, making the entire process more

accessible to a larger population. Using these methods, customizable transparent ceramic structures can be fabricated with greater relative ease and efficiency via 3D printing and vacuum sintering when compared with conventional methods without a significant difference in quality

## **VI. FUTURE WORK**

Additional work in this area could aim towards experimenting with and optimizing the processing parameters further to see if better results can be achieved. As mentioned previously in Section II, each 3D printing parameter is divided into additional subgroups, but these subgroups were held constant for consistency. By experimenting with each subgroup parameter, higher quality parts can potentially be produced in a more efficient manner. Furthermore, for the sintering parameters, different combinations of temperatures and hold times can be investigated in the two-step sintering profiles to achieve higher densities and smaller grain sizes. Although post-HIP treatment was not used in this work, it has been widely demonstrated in literature to improve the properties of optical ceramics and can also be implemented in this process following vacuum sintering.

Due to the versatile nature of the 3D printer used in this work, nearly any ceramic which can be incorporated into a printable slurry may be compatible with this process. So, although only  $\text{Al}_2\text{O}_3$  was used in this work, other transparent ceramic materials, such as  $\text{Y}_2\text{O}_3$ , YAG, and others along with different dopants could be explored as well. Such materials may yield more functional ceramic parts to be produced via 3D printing, such as solid-state lasers and scintillating devices.

In this thesis, the main focus was on the optical properties of the ceramics, with no testing or measurements made regarding the mechanical, thermal, and electrical properties. Such testing may be an additional area of interest for many researchers to evaluate and see if 3D printing is still comparable to conventional processing methods in that regard. So, although the main goals of this research were accomplished, there is still much work in this area that may be accomplished in the future.

## VII. REFERENCES

1. Coble, R. L. Transparent alumina and method of preparation. US3026210A, March 20, 1962.
2. Goldstein, A.; Krell, A.; Kleebe, A., Transparent Ceramics at 50: Progress Made and Further Prospects. *J. Am. Ceram. Soc.* **2016**, *99* (10), 3173-3197.
3. Burke, J. E., Lucalox Alumina: The Ceramic That Revolutionized Outdoor Lighting. *MRS Bull.* **1996**, *21* (6), 61-68.
4. Salem, J. A., Transparent Armor Ceramics as Spacecraft Windows. *J. Am. Ceram. Soc.* **2013**, *96* (1), 281-289.
5. Liu, X. J.; Chen, F.; Zhang, F.; Zhang, H. L.; Zhang, Z.; Wang, J.; Wang, S. W.; Huang, Z. R., Hard transparent AlON ceramic for visible/IR windows. *Int. J. Refract. Met. Hard Mater.* **2013**, *39*, 38-43.
6. Sanghera, J.; Kim, W.; Villalobos, G.; Shaw, B.; Baker, C.; Frantz, J.; Sadowski, B.; Aggarwal, I., Ceramic Laser Materials. *Mater.* **2012**, *5* (2), 258-277.
7. Sanghera, J.; Bayya, S.; Villalobos, G.; Kim, W.; Frantz, J.; Shaw, B.; Sadowski, B.; Miklos, R.; Baker, C.; Hunt, M.; Aggarwal, I.; Kung, F.; Reicher, D.; Peplinski, S.; Ogloza, A.; Langston, P.; Lamar, C.; Varmette, P.; Dubinskiy, M.; DeSandre, L., Transparent ceramics for high-energy laser systems. *Opt. Mater. (Amsterdam, Neth.)* **2011**, *33* (3), 511-518.
8. Strassburger, E., Ballistic testing of transparent armour ceramics. *J. Eur. Ceram. Soc.* **2009**, *29* (2), 267-273.
9. Suárez, M.; Fernández, A.; Torrecillas, R.; Menéndez, J., Sintering to Transparency of Polycrystalline Ceramic Materials. In *Sintering of Ceramics - New Emerging Techniques*, Lakshmanan, A., Ed. InTech: Rijeka, Croatia, 2012; pp 527-553.
10. Wang, S. F.; Zhang, J.; Luo, D. W.; Gu, F.; Tang, D. Y.; Dong, Z. L.; Tan, G. E. B.; Que, W. X.; Zhang, T. S.; Li, S.; Kong, L. B., Transparent ceramics: Processing, materials and applications. *Progress in Solid State Chemistry* **2013**, *41* (1), 20-54.
11. Xiao, Z.; Yu, S.; Li, Y.; Ruan, S.; Kong, L. B.; Huang, Q.; Huang, Z.; Zhou, K.; Su, H.; Yao, Z.; Que, W.; Liu, Y.; Zhang, T.; Wang, J.; Liu, P.; Shen, D.; Allix, M.; Zhang, J.; Tang, D., Materials development and potential applications of transparent ceramics: A review. *Materials Science and Engineering: R: Reports* **2020**, *139*, 100518.

12. Xiao, Z.; Yu, S.; Li, Y.; Ruan, S.; Kong, L. B.; Huang, Q.; Huang, Z.; Zhou, K.; Su, H.; Yao, Z.; Que, W.; Liu, Y.; Zhang, T.; Wang, J.; Liu, P.; Shen, D.; Allix, M.; Zhang, J.; Tang, D., Materials development and potential applications of transparent ceramics: A review. *Mater. Sci. Eng. R Rep.* **2020**, *139*, 100518.
13. Ikesue, A.; Aung, Y.; Taira, T.; Kamimura, T.; Yoshida, K.; Messing, G., Progress In Ceramic Lasers. *Annu. Rev. Mater. Res* **2006**, *17* (36), 397-429.
14. Peelen, J. G. J.; Metselaar, R., Light scattering by pores in polycrystalline materials: Transmission properties of alumina. *J. Appl. Phys. (Melville, NY, U.S.)* **1974**, *45* (1), 216-220.
15. Chen, S.; Wu, Y., New Opportunities for Transparent Ceramics. *Am. Ceram. Soc. Bull.* **2013**, *92* (2), 32-37.
16. Stuer, M. Transparent Polycrystalline Alumina Processing, Sintering and Microstructural Analysis. EPFL, 2012.
17. Peelen, J. G. J. Alumina : sintering and optical properties. Technische Hogeschool Eindhoven, Eindhoven, 1977.
18. Pille, A.; Amamra, M.; Kanaev, A.; Schoenstein, F., Microstructure and optical properties of alumina sintered from various phases. *Ceram. Int.* **2019**, *45* (7, Part B), 9625-9630.
19. Zhang, X.; Liang, S.; Li, H.; Yang, J., Mechanical and optical properties of transparent alumina obtained by rapid vacuum sintering. *Ceram. Int.* **2017**, *43* (1, Part A), 420-426.
20. Mata-Osoro, G.; Moya, J. S.; Pecharroman, C., Transparent alumina by vacuum sintering. *Journal of the European Ceramic Society* **2012**, *32* (11), 2925-2933.
21. Jones, I. K.; Seeley, Z. M.; Cherepy, N. J.; Duoss, E. B.; Payne, S. A., Direct ink write fabrication of transparent ceramic gain media. *Optical Materials* **2018**, *75*, 19-25.
22. Sarkar, D., *Ceramic processing : industrial practices*. 1st ed.; CRC Press LLC: Boca Raton, FL, 2019; pp 71-101.
23. Wu, Y., Nanostructured transparent ceramics with an anisotropic crystalline structure. *Opt. Mater. Express* **2014**, *4* (10), 2026-2031.
24. Krell, A.; Strassburger, E., Ballistic Strength of Opaque and Transparent Armor. *Am. Ceram. Soc. Bull.* **2007**, *86* (4), 9201-9207.

25. Krell, A.; Blank, P.; Ma, H.; Hutzler, T.; van Bruggen, M. P. B.; Apetz, R., Transparent Sintered Corundum with High Hardness and Strength. *J. Am. Ceram. Soc.* **2003**, *86* (1), 12-18.
26. Grasso, S.; Yoshida, H.; Porwal, H.; Sakka, Y.; Reece, M., Highly transparent  $\alpha$ -alumina obtained by low cost high pressure SPS. *Ceram. Int.* **2013**, *39* (3), 3243-3248.
27. Mata-Osoro, G.; Moya, J. S.; Pecharroman, C., Transparent alumina by vacuum sintering. *J. Eur. Ceram. Soc.* **2012**, *32* (11), 2925-2933.
28. Gentilman, R. L.; Maguire, E. A.; Dolhert, L. E. Transparent aluminum oxynitride and method of manufacture. US4520116A, May 28, 1985.
29. Ramisetty, M.; Sastri, S.; Kashalikar, U.; Goldman, L.; Nag, N., Transparent Polycrystalline Cubic Spinels Protect and Defend. *Am. Ceram. Soc. Bull.* **2013**, *92*, 20-25.
30. Warner, C.; Hartnett, T.; Fisher, D.; Sunne, W., Characterization of ALON (TM) optical ceramic. *Proc. SPIE-Int. Soc. Opt. Eng.* **2005**, 5786.
31. Wahl, J.; Hartnett, T.; Goldman, L.; Twedt, R.; Warner, C. In *Recent advances in ALON optical ceramic*, Defense and Security, Orlando, FL, SPIE: Orlando, FL, 2005.
32. Jiang, N.; Liu, Q.; Xie, T.; Ma, P.; Kou, H.; Pan, Y.; Li, J., Fabrication of highly transparent ALON ceramics by hot isostatic pressing post-treatment. *J. Eur. Ceram. Soc.* **2017**, *37* (13), 4213-4216.
33. Kumar, R. S.; Johnson, R., Aqueous Slip Casting of Transparent Aluminum Oxynitride. *J. Am. Ceram. Soc.* **2016**, *99* (10), 3220-3225.
34. Hartnett, T. M.; Bernstein, S. D.; Maguire, E. A.; Tustison, R. W., Optical properties of ALON (aluminum oxynitride). *Infrared Phys. Technol.* **1998**, *39* (4), 203-211.
35. Frage, N.; Cohen, S.; Meir, S.; Kalabukhov, S.; Dariel, M. P., Spark plasma sintering (SPS) of transparent magnesium-aluminate spinel. *J. Mater. Sci.* **2007**, *42* (9), 3273-3275.
36. Suarez, M.; Rocha, V.; Fernandez, A.; Menendez, J. L.; Torrecillas, R., Synthesis and processing of spinel powders for transparent ceramics. *Ceram. Int.* **2014**, *40* (3), 4065-4069.
37. Tokariev, O.; Schnetter, L.; Beck, T.; Malzbender, J., Grain size effect on the mechanical properties of transparent spinel ceramics. *Journal of the European Ceramic Society* **2013**, *33* (4), 749-757.

38. Khasanov, O.; Dvilis, E.; Khasanov, A.; Polisadova, E.; Kachaev, A., Optical and mechanical properties of transparent polycrystalline MgAl<sub>2</sub>O<sub>4</sub> spinel depending on SPS conditions. *Phys. Status Solidi C* **2013**, *10* (6), 918-920.
39. Anderson, R. C. Transparent yttria-based ceramics and method for producing same. US3545987A, December 8, 1970.
40. Hogan, P.; Stefanik, T.; Willingham, C.; Gentilman, R. In *Transparent Yttria for IR Windows and Domes-Past and Present*, DoD Electromagnetic Windows Symposium, Norfolk, VA, Raytheon Integrated Defense Systems: Norfolk, VA, 2004; pp 1-65.
41. Tropf, W. J.; Harris, D. C. In *Mechanical, Thermal, And Optical Properties Of Yttria And Lanthana-Doped Yttria*, SPIE 1989 Technical Symposium on Aerospace Sensing, Orlando, FL, Klocek, P., Ed. SPIE: Orlando, FL, 1989.
42. Hou, X.; Zhou, S.; Li, W.; Li, Y., Study on the effect and mechanism of zirconia on the sinterability of yttria transparent ceramic. *J. Eur. Ceram. Soc.* **2010**, *30* (15), 3125-3129.
43. Greskovich, C.; Chernoch, J. P., Polycrystalline ceramic lasers. *J. Appl. Phys. (Melville, NY, U.S.)* **1973**, *44* (10), 4599-4606.
44. Kong, J.; Tang, D. Y.; Zhao, B.; Lu, J.; Ueda, K.; Yagi, H.; Yanagitani, T., 9.2-W diode-end-pumped Yb:Y<sub>2</sub>O<sub>3</sub> ceramic laser. *Appl. Phys. Lett.* **2005**, *86* (16), 161116-161116-3.
45. Petermann, K., Oxide laser crystals doped with rare earth and transition metal ions. In *Handbook of Solid-State Lasers*, 1st ed.; Denker, B.; Shklovsky, E., Eds. Woodhead Publishing Limited: Cambridge, UK, 2013; pp 3-27.
46. Ikesue, A., Polycrystalline Nd:YAG ceramics lasers. *Opt. Mater. (Amsterdam, Neth.)* **2002**, *19* (1), 183-187.
47. Ikesue, A.; Kinoshita, T.; Kamata, K.; Yoshida, K., Fabrication and Optical Properties of High-Performance Polycrystalline Nd:YAG Ceramics for Solid-State Lasers. *J. Am. Ceram. Soc.* **1995**, *78* (4), 1033-1040.
48. Ikesue, A.; Yoshida, K.; Yamamoto, T.; Yamaga, I., Optical Scattering Centers in Polycrystalline Nd:YAG Laser. *J. Am. Ceram. Soc.* **1997**, *80* (6), 1517-1522.
49. Zhou, T.; Zhang, L.; Wei, S.; Wang, L.; Yang, H.; Fu, Z.; Chen, H.; Selim, F. A.; Zhang, Q., MgO assisted densification of highly transparent YAG ceramics and their microstructural evolution. *J. Eur. Ceram. Soc.* **2018**, *38* (2), 687-693.

50. Wagner, A.; Ratzker, B.; Kalabukhov, S.; Sokol, M.; Frage, N., Residual porosity and optical properties of spark plasma sintered transparent polycrystalline cerium-doped YAG. *J. Eur. Ceram. Soc.* **2019**, *39* (4), 1436-1442.
51. Kochawattana, S.; Stevenson, A.; Lee, S.-H.; Ramirez, M.; Gopalan, V.; Dumm, J.; Castillo, V. K.; Quarles, G. J.; Messing, G. L., Sintering and grain growth in SiO<sub>2</sub> doped Nd:YAG. *J. Eur. Ceram. Soc.* **2008**, *28* (7), 1527-1534.
52. Ikesue, A.; Furusato, I.; Kamata, K., Fabrication of Polycrystalline, Transparent YAG Ceramics by a Solid-State Reaction Method. *J. Am. Ceram. Soc.* **1995**, *78* (1), 225-228.
53. Lee, S.-H.; Kochawattana, S.; Messing, G. L.; Dumm, J. Q.; Quarles, G.; Castillo, V., Solid-State Reactive Sintering of Transparent Polycrystalline Nd:YAG Ceramics. *J. Am. Ceram. Soc.* **2006**, *89* (6), 1945-1950.
54. Li, J.; Chen, F.; Liu, W.; Zhang, W.; Wang, L.; Ba, X.; Zhu, Y.; Pan, Y.; Guo, J., Co-precipitation synthesis route to yttrium aluminum garnet (YAG) transparent ceramics. *J. Eur. Ceram. Soc.* **2012**, *32* (11), 2971-2979.
55. Li, H.-L.; Liu, X.-J.; Xie, R.-J.; Zeng, Y.; Ping Huang, L., Fabrication of Transparent Cerium-Doped Lutetium Aluminum Garnet Ceramics by Co-Precipitation Routes. *J. Am. Ceram. Soc.* **2006**, *89* (7), 2356-2358.
56. Zhang, W.; Lu, T. C.; Wei, N.; Shi, Y. L.; Ma, B. Y.; Luo, H.; Zhang, Z. B.; Deng, J.; Guan, Z. G.; Zhang, H. R.; Li, C. N.; Niu, R. H., Co-precipitation synthesis and vacuum sintering of Nd:YAG powders for transparent ceramics. *Mater. Res. Bull.* **2015**, *70*, 365-372.
57. Dupont, A.; Parent, C.; Le Garrec, B.; Heintz, J. M., Size and morphology control of Y<sub>2</sub>O<sub>3</sub> nanopowders via a sol-gel route. *J. Solid State Chem.* **2003**, *171* (1), 152-160.
58. Balabanov, S. S.; Yavetskiy, R. P.; Belyaev, A. V.; Gavrishchuk, E. M.; Drobotenko, V. V.; Evdokimov, I. I.; Novikova, A. V.; Palashov, O. V.; Permin, D. A.; Pimenov, V. G., Fabrication of transparent MgAl<sub>2</sub>O<sub>4</sub> ceramics by hot-pressing of sol-gel-derived nanopowders. *Ceram. Int.* **2015**, *41* (10, Part A), 13366-13371.
59. Hajizadeh-Oghaz, M.; Razavi, R. S.; Barekat, M.; Naderi, M.; Malekzadeh, S.; Rezazadeh, M., Synthesis and characterization of Y<sub>2</sub>O<sub>3</sub> nanoparticles by sol-gel process for transparent ceramics applications. *J. Sol-Gel Sci. Technol.* **2016**, *78* (3), 682-691.
60. Nunes, D.; Pimentel, A.; Santos, L.; Barquinha, P.; Pereira, L.; Fortunato, E.; Martins, R., Synthesis, design, and morphology of metal oxide nanostructures. In *Metal Oxide Nanostructures*, 1st ed.; Korotcenkov, G.; Eds. Elsevier: Amsterdam, 2019; pp 21-57.

61. Teoh, W. Y.; Amal, R.; Madler, L., Flame spray pyrolysis: An enabling technology for nanoparticles design and fabrication. *Nanoscale* **2010**, *2* (8), 1324-1347.
62. Jones, I. K.; Seeley, Z. M.; Cherepy, N. J.; Duoss, E. B.; Payne, S. A., Direct ink write fabrication of transparent ceramic gain media. *Opt. Mater. (Amsterdam, Neth.)* **2018**, *75*, 19-25.
63. Katz, A.; Barraud, E.; Lemonnier, S.; Sorrel, E.; Boehmler, J.; Blanc, A.; Eichhorn, M.; d'Astorg, S.; Leriche, A., Influence of powder physicochemical characteristics on microstructural and optical aspects of YAG and Er:YAG ceramics obtained by SPS. *Ceram. Int.* **2017**, *43* (14), 10673-10682.
64. Baklouti, S.; Chartier, T.; Baumard, J. F.; Coupelle, P. In *Uniaxial pressing of spray-dried alumina agglomerates*, Conference: 5. international conference on ceramic processing science and technology, Friedrichsafen, Germany, American Ceramic Society, Westerville, OH (United States): Friedrichsafen, Germany, 1995; pp 271-275.
65. Baklouti, S.; Chartier, T.; Gault, C.; Baumard, J. F., The effect of binders on the strength and Young's modulus of dry pressed alumina. *J. Eur. Ceram. Soc.* **1998**, *18* (4), 323-328.
66. Zheng, J.; Reed, J. S., Particle and Granule Parameters Affecting Compaction Efficiency in Dry Pressing. *J. Am. Ceram. Soc.* **1988**, *71* (11), C456-C458.
67. Walker Jr., W. J.; Reed, J. S.; Verma, S. K., Polyethylene Glycol Binders for Advanced Ceramics. In *A Collection of Papers on Engineering Aspects of Fabrication of Ceramics: Ceramic Engineering and Science Proceedings*, 11/12 ed.; Wachtman, J. B. J., Ed. The American Ceramics Society: Westerville, OH, 1993; Vol. 14, pp 58-79.
68. An, S.-M.; Kang, S.-J. L., Boundary structural transition and grain growth behavior in BaTiO<sub>3</sub> with Nd<sub>2</sub>O<sub>3</sub> doping and oxygen partial pressure change. *Acta Mater.* **2011**, *59* (5), 1964-1973.
69. Varela, J. A.; Whitemore, O. J.; Longo, E., Pore size evolution during sintering of ceramic oxides. *Ceram. Int.* **1990**, *16* (3), 177-189.
70. Thompson, A. M.; Harmer, M. P., Influence of Atmosphere on the Final-Stage Sintering Kinetics of Ultra-High-Purity Alumina. *J. Am. Ceram. Soc.* **1993**, *76* (9), 2248-2256.
71. Zhang, W. X.; Zhou, J.; Liu, W. B.; Li, J.; Wang, L.; Jiang, B. X.; Pan, Y. B.; Cheng, X. J.; Xu, J. Q., Fabrication, properties and laser performance of Ho:YAG transparent ceramic. *J. Alloys Compd.* **2010**, *506* (2), 745-748.

72. Ge, L.; Li, J.; Zhou, Z.; Liu, B.; Xie, T.; Liu, J.; Kou, H.; Shi, Y.; Pan, Y.; Guo, J., Nd:YAG transparent ceramics fabricated by direct cold isostatic pressing and vacuum sintering. *Opt. Mater. (Amsterdam, Neth.)* **2015**, *50*, 25-31.
73. Tokariev, O.; Schnetter, L.; Beck, T.; Malzbender, J., Grain size effect on the mechanical properties of transparent spinel ceramics. *J. Eur. Ceram. Soc.* **2013**, *33* (4), 749-757.
74. Guillon, O.; Gonzalez-Julian, J.; Dargatz, B.; Kessel, T.; Schierning, G.; Räthel, J.; Herrmann, M., Field-Assisted Sintering Technology/Spark Plasma Sintering: Mechanisms, Materials, and Technology Developments. *Adv. Eng. Mater.* **2014**, *16* (7), 830-849.
75. Schlup, A. P.; Costakis Jr., W. J.; Rheinheimer, W.; Trice, R. W.; Youngblood, J. P., Hot-pressing platelet alumina to transparency. *J. Am. Ceram. Soc.* **2020**, *103* (4), 2587-2601.
76. Zhang, G.; Carloni, D.; Wu, Y., Ultraviolet emission transparent Gd:YAG ceramics processed by solid-state reaction spark plasma sintering. *J. Am. Ceram. Soc.* **2020**, *103* (2), 839-848.
77. Talimian, A.; Pouchly, V.; El-Maghraby, H. F.; Maca, K.; Galusek, D., Transparent magnesium aluminate spinel: Effect of critical temperature in two-stage spark plasma sintering. *J. Eur. Ceram. Soc.* **2020**.
78. Yang, J.; Yu, J.; Huang, Y., Recent developments in gelcasting of ceramics. *J. Eur. Ceram. Soc.* **2011**, *31* (14), 2569-2591.
79. Gauckler, L. J.; Graule, T.; Baader, F., Ceramic forming using enzyme catalyzed reactions. *Mater. Chem. Phys.* **1999**, *61* (1), 78-102.
80. Gilissen, R.; Erauw, J. P.; Smolders, A.; Vanswijgenhoven, E.; Luyten, J., Gelcasting, a near net shape technique. *Mater. Des.* **2000**, *21* (4), 251-257.
81. Jabbari, M.; Bulatova, R.; Tok, A. I. Y.; Bahl, C. R. H.; Mitsoulis, E.; Hattel, J. H., Ceramic tape casting: A review of current methods and trends with emphasis on rheological behaviour and flow analysis. *Mater. Sci. Eng., B* **2016**, *212*, 39-61.
82. Appiagyeyi, K. A.; Messing, G. L.; Dumm, J. Q., Aqueous slip casting of transparent yttrium aluminum garnet (YAG) ceramics. *Ceram. Int.* **2008**, *34* (5), 1309-1313.
83. Liu, Y.; Zhu, J., Fabrication of transparent MgAl<sub>2</sub>O<sub>4</sub> ceramics by gelcasting and cold isostatic pressing. *Ceram. Int.* **2020**, *46* (4), 4154-4158.

84. Jin, L.; Zhou, G.; Shimai, S.; Zhang, J.; Wang, S., ZrO<sub>2</sub>-doped Y<sub>2</sub>O<sub>3</sub> transparent ceramics via slip casting and vacuum sintering. *J. Eur. Ceram. Soc.* **2010**, *30* (10), 2139-2143.
85. Zhang, W.; Lu, T.; Ma, B.; Wei, N.; Lu, Z.; Li, F.; Guan, Y.; Chen, X.; Liu, W.; Qi, L., Improvement of optical properties of Nd:YAG transparent ceramics by post-annealing and post hot isostatic pressing. *Opt. Mater. (Amsterdam, Neth.)* **2013**, *35* (12), 2405-2410.
86. Hirano, M.; Inagaki, M.; Mizutani, Y.; Nomura, K.; Kawai, M.; Nakamura, Y., Improvement of Mechanical and Electrical Properties of Scandia-Doped Zirconia Ceramics by Post-Sintering with Hot Isostatic Pressing. *J. Am. Ceram. Soc.* **2000**, *83* (10), 2619-2621.
87. Chrétien, L.; Boulesteix, R.; Maître, A.; Sallé, C.; Reignoux, Y., Post-sintering treatment of neodymium-doped yttrium aluminum garnet (Nd:YAG) transparent ceramics. *Opt. Mater. Express* **2014**, *4* (10), 2166-2173.
88. Wang, Z.; Zhang, L.; Yang, H.; Zhang, J.; Wang, L.; Zhang, Q., High optical quality Y<sub>2</sub>O<sub>3</sub> transparent ceramics with fine grain size fabricated by low temperature air pre-sintering and post-HIP treatment. *Ceram. Int.* **2016**, *42* (3), 4238-4245.
89. Luo, W.; Ma, P.; Xie, T.; Dai, J.; Pan, Y.; Kou, H.; Li, J., Fabrication and spectroscopic properties of Co:MgAl<sub>2</sub>O<sub>4</sub> transparent ceramics by the HIP post-treatment. *Opt. Mater. (Amsterdam, Neth.)* **2017**, *69*, 152-157.
90. Fu, Y.; Li, J.; Liu, Y.; Liu, L.; Zhao, H.; Pan, Y., Effect of air annealing on the optical properties and laser performance of Nd:YAG transparent ceramics. *Opt. Mater. Express* **2014**, *4* (10), 2108-2115.
91. Zhang, W.; Lu, T.; Wei, N.; Ma, B.; Li, F.; Lu, Z.; Qi, J., Effect of annealing on the optical properties of Nd:YAG transparent ceramics. *Opt. Mater. (Amsterdam, Neth.)* **2012**, *34* (4), 685-690.
92. Zhang, W.; Lu, T.; Ma, B.; Wei, N.; Lu, Z.; Li, F.; Guan, Y.; Chen, X.; Liu, W.; Qi, L., Improvement of optical properties of Nd:YAG transparent ceramics by post-annealing and post hot isostatic pressing. *Optical Materials* **2013**, *35* (12), 2405-2410.
93. Li, J.; Zhu, Y.; Chen, C. T., Chemical Mechanical Polishing of Transparent Nd:YAG Ceramics. *Key Eng. Mater.* **2008**, *375-376*, 278-282.
94. Marinescu, I. D.; Uhlmann, E.; Doi, T. K., *Handbook of lapping and polishing*. 1st ed.; CRC Press LLC: Baton Rouge, LA, 2006; pp 7-341.

95. Ross, D.; Wang, Y.; Ramadhan, H.; Yamaguchi, H., Polishing Characteristics of Transparent Polycrystalline Yttrium Aluminum Garnet Ceramics Using Magnetic Field-Assisted Finishing. *J. Micro. Nanomanuf.* **2016**, *4* (4), 041007.
96. Golini, D.; Jacobs, S.; Kordonski, W.; Dumas, P., *Precision optics fabrication using magnetorheological finishing*. SPIE: 1997; Vol. 10289.
97. Ngo, T.; Kashani, A.; Imbalzano, G.; Nguyen, K.; Hui, D., Additive manufacturing (3D printing): A review of materials, methods, applications and challenges. *Composites, Part B* **2018**, *143*.
98. Lu, B.; Li, D.; Tian, X., Development Trends in Additive Manufacturing and 3D Printing. *Engineering* **2015**, *1* (1), 85-89.
99. Wong, K. V.; Hernandez, A., A Review of Additive Manufacturing. *ISRN Mech. Eng.* **2012**, *2012* (4), 1-10.
100. Chen, Z.; Li, Z.; Li, J.; Liu, C.; Lao, C.; Fu, Y.; Liu, C.; Li, Y.; Wang, P.; He, Y., 3D printing of ceramics: A review. *J. Eur. Ceram. Soc.* **2019**, *39* (4), 661-687.
101. Zocca, A.; Colombo, P.; Gomes, C. M.; Günster, J., Additive Manufacturing of Ceramics: Issues, Potentialities, and Opportunities. *J. Am. Ceram. Soc.* **2015**, *98* (7), 1983-2001.
102. Bechthold, M., Ceramic prototypes - design, computation, and digital fabrication. *Inf. Constr.* **2016**, *68* (544), 1-11.
103. Marcus, H. L.; Beaman, J. J.; Barlow, J. W.; Bourell, D. L., Solid freeform fabrication. Powder processing. *Am. Ceram. Soc. Bull.* **1990**, *69* (6), 1030-1031.
104. Sachs, E.; Cima, M.; Cornie, J., Three-Dimensional Printing: Rapid Tooling and Prototypes Directly from a CAD Model. *CIRP Ann.* **1990**, *39* (1), 201-204.
105. Cesarano, I., Joseph; Calvert, P. D. Freeforming objects with low-binder slurry. US 6027326, January 1, 2000.
106. Cesarano, J.; Segalman, R.; Calvert, P. W., Robocasting provides moldless fabrication from slurry deposition. *Ceram. Ind. (Troy, MI, U.S.)* **1998**, *148* (4), 94-100.
107. Li, J. P.; Habibovic, P.; van den Doel, M.; Wilson, C. E.; de Wijn, J. R.; van Blitterswijk, C. A.; de Groot, K., Bone ingrowth in porous titanium implants produced by 3D fiber deposition. *Biomaterials* **2007**, *28* (18), 2810-2820.
108. Smay, J. E.; Gratson, G. M.; Shepherd, R. F.; Cesarano III, J.; Lewis, J. A., Directed Colloidal Assembly of 3D Periodic Structures. *Adv. Mater.* **2002**, *14* (18), 1279-1283.

109. Smay, J. E.; Cesarano, J.; Lewis, J. A., Colloidal Inks for Directed Assembly of 3-D Periodic Structures. *Langmuir* **2002**, *18* (14), 5429-5437.
110. Miranda, P.; Saiz, E.; Gryn, K.; Tomsia, A. P., Sintering and robocasting of beta-tricalcium phosphate scaffolds for orthopaedic applications. *Acta Biomater.* **2006**, *2* (4), 457-66.
111. Martínez-Vázquez, F. J.; Perera, F. H.; Miranda, P.; Pajares, A.; Guiberteau, F., Improving the compressive strength of bioceramic robocast scaffolds by polymer infiltration. *Acta Biomater.* **2010**, *6* (11), 4361-4368.
112. Eqtesadi, S.; Motealleh, A.; Miranda, P.; Lemos, A.; Rebelo, A.; Ferreira, J. M. F., A simple recipe for direct writing complex 45S5 Bioglass® 3D scaffolds. *Mater. Lett.* **2013**, *93*, 68-71.
113. Elsayed, H.; Colombo, P.; Bernardo, E., Direct ink writing of wollastonite-diopside glass-ceramic scaffolds from a silicone resin and engineered fillers. *J. Eur. Ceram. Soc.* **2017**, *37* (13), 4187-4195.
114. Michna, S.; Wu, W.; Lewis, J. A., Concentrated hydroxyapatite inks for direct-write assembly of 3-D periodic scaffolds. *Biomater.* **2005**, *26* (28), 5632-5639.
115. Simon, J. L.; Michna, S.; Lewis, J. A.; Rekow, E. D.; Thompson, V. P.; Smay, J. E.; Yampolsky, A.; Parsons, J. R.; Ricci, J. L., In vivo bone response to 3D periodic hydroxyapatite scaffolds assembled by direct ink writing. *J. Biomed. Mater. Res., Part A* **2007**, *83* (3), 747-58.
116. Zocca, A.; Franchin, G.; Elsayed, H.; Gioffredi, E.; Bernardo, E.; Colombo, P., Direct Ink Writing of a Pre-ceramic Polymer and Fillers to Produce Hardystonite (Ca<sub>2</sub>ZnSi<sub>2</sub>O<sub>7</sub>) Bioceramic Scaffolds. *J. Am. Ceram. Soc.* **2016**, *99* (6), 1960-1967.
117. Stuecker, J. N.; Miller, J. E.; Ferrizz, R. E.; Mudd, J. E.; Cesarano, J., Advanced Support Structures for Enhanced Catalytic Activity. *Ind. Eng. Chem. Res.* **2004**, *43* (1), 51-55.
118. Kuhn, M.; Napporn, T.; Meunier, M.; Vengallatore, S.; Therriault, D., Direct-write microfabrication of single-chamber micro solid oxide fuel cells. *J. Micromech. Microeng.* **2007**, *238* (18), 015005.
119. Sun, K.; Wei, T.-S.; Ahn, B. Y.; Seo, J. Y.; Dillon, S. J.; Lewis, J. A., 3D Printing of Interdigitated Li-Ion Microbattery Architectures. *Adv. Mater.* **2013**, *25* (33), 4539-4543.

120. Liu, C.; Cheng, X.; Li, B.; Chen, Z.; Mi, S.; Lao, C., Fabrication and Characterization of 3D-Printed Highly-Porous 3D LiFePO<sub>4</sub> Electrodes by Low Temperature Direct Writing Process. *Materials* **2017**, *10* (8), 934.
121. Blazdell, P. F.; Evans, J. R. G.; Edirisinghe, M. J.; Shaw, P.; Binstead, M. J., The computer aided manufacture of ceramics using multilayer jet printing. *J. Mater. Sci. Lett.* **1995**, *14* (22), 1562-1565.
122. Xiang, Q. F.; Evans, J. R. G.; Edirisinghe, M. J.; Blazdell, P. F., Solid freeforming of ceramics using a drop-on-demand jet printer. *Proc. Inst. Mech. Eng., Part B* **1997**, *211* (3), 211-214.
123. Hull, C. W. Apparatus For Production Of Three-dimensional Objects By Stereolithography. US4575330A, August 8, 1984.
124. Cooper, K., *Rapid Prototyping Technology: Selection and Application*. 1st ed.; CRC Press: Boca Raton, FL, 2001; Vol. 1, pp 59-118.
125. Kim, H., Scheduling and process planning for multiple material stereolithography. *Rapid Prototyp. J.* **2010**, *16* (4), 232-240.
126. Pham, D.; Ji, C., Design for stereolithography. *Proc. Inst. Mech. Eng. C* **2000**, *214* (5), 635-640.
127. Nguyen, N. T.; Delhote, N.; Ettore, M.; Baillargeat, D.; Le Coq, L.; Sauleau, R., Design and Characterization of 60-GHz Integrated Lens Antennas Fabricated Through Ceramic Stereolithography. *IEEE Trans. Antennas Propag.* **2010**, *58* (8), 2757-2762.
128. Kirihara, S.; Niki, T., Three-Dimensional Stereolithography of Alumina Photonic Crystals for Terahertz Wave Localization. *Int. J. Appl. Ceram. Technol.* **2015**, *12* (1), 32-37.
129. Scalera, F.; Esposito Corcione, C.; Montagna, F.; Sannino, A.; Maffezzoli, A., Development and characterization of UV curable epoxy/hydroxyapatite suspensions for stereolithography applied to bone tissue engineering. *Ceram. Int.* **2014**, *40* (10, Part A), 15455-15462.
130. Du, D.; Asaoka, T.; Ushida, T.; Furukawa, K. S., Fabrication and perfusion culture of anatomically shaped artificial bone using stereolithography. *Biofabrication* **2014**, *6* (4), 045002.
131. He, R.; Liu, W.; Wu, Z.; An, D.; Huang, M.; Wu, H.; Jiang, Q.; Ji, X.; Wu, S.; Xie, Z., Fabrication of complex-shaped zirconia ceramic parts via a DLP-stereolithography-based 3D printing method. *Ceram. Int.* **2018**, *44* (3), 3412-3416.

132. Scheithauer, U.; Schwarzer, E.; Moritz, T.; Michaelis, A., Additive Manufacturing of Ceramic Heat Exchanger: Opportunities and Limits of the Lithography-Based Ceramic Manufacturing (LCM). *J. Mater. Eng. Perform.* **2017**, *27* (12), 14-20.
133. Tiller, B.; Reid, A.; Zhu, B.; Guerreiro, J.; Domingo-Roca, R.; Curt Jackson, J.; Windmill, J. F. C., Piezoelectric microphone via a digital light processing 3D printing process. *Mater. Des.* **2019**, *165*, 107593.
134. Sun, H.-B.; Kawata, S., Two-Photon Photopolymerization and 3D Lithographic Microfabrication. In *NMR-3D Analysis-Photopolymerization*, Lee, K.-S., Ed. Springer-Verlag: Berlin, Germany, 2004; Vol. 170, pp 169-273.
135. Borisov, R. A.; Dorozhkina, G.; Koroteev, N. I.; Kozenkov, V. M.; Magnitskiy, S.; Malakhov, D. V.; Tarasishin, A. V.; Zheltikov, A. M., Fabrication of three-dimensional periodic microstructures by means of two-photon polymerization. *Appl. Phys. B: Lasers Opt.* **1998**, *67* (6), 765-767.
136. Kawata, S.; Sun, H.-B.; Tanaka, T.; Takada, K., Finer features for functional microdevices. *Nature* **2001**, *412* (6848), 697-698.
137. Sun, H.-B.; Matsuo, S.; Misawa, H., Three-dimensional photonic crystal structures achieved with two-photon-absorption photopolymerization of resin. *Appl. Phys. Lett.* **1999**, *74* (6), 786-788.
138. Cumpston, B. H.; Ananthavel, S. P.; Barlow, S.; Dyer, D. L.; Ehrlich, J. E.; Erskine, L. L.; Heikal, A. A.; Kuebler, S. M.; Lee, I. Y. S.; McCord-Maughon, D.; Qin, J.; Röckel, H.; Rumi, M.; Wu, X.-L.; Marder, S. R.; Perry, J. W., Two-photon polymerization initiators for three-dimensional optical data storage and microfabrication. *Nature* **1999**, *398* (6722), 51-54.
139. Yang, H.-K.; Kim, M. J.; Kang, S.-W.; Kim, K.-S.; Lee, K.-S.; Hu Park, S.; Yang, D.-Y.; Kong, H. J.; Sun, H.-B.; Kawata, S.; Fleits, P., Recent Progress of Lithographic Microfabrication by the TPA-Induced Photopolymerization. *J. Photopolym. Sci. Technol.* **2004**, *17* (3), 385-392.
140. Takada, K.; Sun, H.-B.; Kawata, S., Improved spatial resolution and surface roughness in photopolymerization-based laser nanowriting. *Appl. Phys. Lett.* **2005**, *86* (7), 071122-071122-3.
141. Seet, K. K.; Mizeikis, V.; Matsuo, S.; Juodkazis, S.; Misawa, H., Three-Dimensional Spiral-Architecture Photonic Crystals Obtained By Direct Laser Writing. *Adv. Mater.* **2005**, *17* (5), 541-545.
142. Pham, T. A.; Kim, D.-P.; Lim, T.-W.; Park, S.-H.; Yang, D.-Y.; Lee, K.-S., Three-Dimensional SiCN Ceramic Microstructures via Nano-Stereolithography of Inorganic Polymer Photoresists. *Adv. Funct. Mater.* **2006**, *16* (9), 1235-1241.

143. Utela, B.; Storti, D.; Anderson, R.; Ganter, M., A review of process development steps for new material systems in three dimensional printing (3DP). *J. Manuf. Process.* **2008**, *10* (2), 96-104.
144. Deckard Carl, R. Method And Apparatus For Producing Parts By Selective Sintering. US4863538A, October 17, 1986.
145. Lakshminarayan, U.; Ogrzydiziak, S.; Marcus, H. L. In *Selective Laser Sintering of Ceramic Materials*, 1990 International Solid Freeform Fabrication Symposium, Austin, TX, Austin, U. o. T. a., Ed. University of Texas at Austin: Austin, TX, 1990; pp 16-26.
146. Lakshminarayan, U.; Marcus, H. L. In *Microstructural and Mechanical Properties of Al<sub>2</sub>O<sub>3</sub>/P<sub>2</sub>O<sub>5</sub> AND Al<sub>2</sub>O<sub>3</sub>/B<sub>2</sub>O<sub>3</sub> Composites Fabricated by Selective Laser Sintering*, 1991 International Solid Freeform Fabrication Symposium, Austin, TX, Austin, U. o. T. a., Ed. University of Texas at Austin: Austin, TX, 1991; pp 205-212.
147. Deckers, J.; Kruth, J.-P.; Shahzad, K.; Vleugels, J., Density improvement of alumina parts produced through selective laser sintering of alumina-polyamide composite powder. *CIRP Ann.* **2012**, *61* (1), 211-214.
148. Deckers, J.; Shahzad, K.; Vleugels, J.; Kruth, J.-P., Isostatic pressing assisted indirect selective laser sintering of alumina components. *Rapid Prototyp. J.* **2012**, *18* (5), 409-419.
149. Deckers Jan, P., Shaping ceramics through indirect selective laser sintering. *Rapid Prototyp. J.* **2016**, *22* (3), 544-558.
150. Shahzad, K.; Deckers, J.; Boury, S.; Neirinck, B.; Kruth, J.-P.; Vleugels, J., Preparation and indirect selective laser sintering of alumina/PA microspheres. *Ceram. Int.* **2012**, *38* (2), 1241-1247.
151. Shahzad, K.; Deckers, J.; Kruth, J.-P.; Vleugels, J., Additive manufacturing of alumina parts by indirect selective laser sintering and post processing. *J. Mater. Process. Technol.* **2013**, *213* (9), 1484-1494.
152. Shahzad, K.; Deckers, J.; Zhang, Z.; Kruth, J.-P.; Vleugels, J., Additive manufacturing of zirconia parts by indirect selective laser sintering. *J. Eur. Ceram. Soc.* **2014**, *34* (1), 81-89.
153. Schleifenbaum, H.; Meiners, W.; Wissenbach, K.; Hinke, C., Individualized production by means of high power Selective Laser Melting. *CIRP J. Manuf. Sci. Tec.* **2010**, *2* (3), 161-169.

154. Lee, H.; Lim, C. H. J.; Low, M. J.; Tham, N.; Murukeshan, V. M.; Kim, Y.-J., Lasers in additive manufacturing: A review. *Int. J. Pr. Eng. Man.-G.T.* **2017**, *4* (3), 307-322.
155. Hao, L.; Dadbakhsh, S.; Seaman, O.; Felstead, M., Selective laser melting of a stainless steel and hydroxyapatite composite for load-bearing implant development. *J. Mater. Process. Technol.* **2009**, *209* (17), 5793-5801.
156. Mercelis, P.; Kruth, J.-P., Residual stresses in Selective Laser Sintering and Selective Laser Melting. *16th Solid Freeform Fabr. Symp. Proc.* **2006**, *12*, 254-265.
157. Shishkovsky, I.; Yadroitsev, I.; Bertrand, P.; Smurov, I., Alumina–zirconium ceramics synthesis by selective laser sintering/melting. *Appl. Surf. Sci.* **2007**, *254* (4), 966-970.
158. Deckers, J.; Meyers, S.; Kruth, J. P.; Vleugels, J., Direct Selective Laser Sintering/Melting of High Density Alumina Powder Layers at Elevated Temperatures. *Phys. Procedia* **2014**, *56*, 117-124.
159. Aggarangsi, P.; Beuth, J. L. In *Localized Preheating Approaches for Reducing Residual Stress in Additive Manufacturing*, 2006 International Solid Freeform Fabrication Symposium, Austin, TX, University of Texas at Austin: Austin, TX, 2006; pp 709-720.
160. Wilkes, J., Additive manufacturing of ZrO<sub>2</sub>-Al<sub>2</sub>O<sub>3</sub> ceramic components by selective laser melting. *Rapid Prototyp. J.* **2013**, *19* (1), 51-57.
161. Exner, H.; Horn, M.; Streek, A.; Ullmann, F.; Hartwig, L.; Regenfuss, P.; Ebert, R., Laser micro sintering: A new method to generate metal and ceramic parts of high resolution with sub-micrometer powder. *Virtual Phys. Prototyp.* **2008**, *3*, 3-11.
162. Exner, H.; Regenfuss, P.; Hartwig, L.; Klötzer, S.; Ebert, R., Selective Laser Micro Sintering with a Novel Process. *Proc. SPIE-Int. Soc. Opt. Eng.* **2003**, *5063*, 145-151.
163. Hagedorn, Y. C.; Balachandran, N.; Meiners, W.; Wissenbach, K.; Poprawet, R., SLM of net-shaped high strength ceramics: New opportunities for producing dental restorations. *22nd Solid Freeform Fabr. Symp. Proc.* **2011**, 536-546.
164. Gibson, I.; Rosen, D. W.; Stucker, B., *Additive Manufacturing Technologies: 3D Printing, Rapid Prototyping, and Direct Digital Manufacturing*. 2nd ed.; Springer Publishing Company, Incorporated: New York, NY, 2009; pp 1-459.
165. Balla, V. K.; Bose, S.; Bandyopadhyay, A., Processing of Bulk Alumina Ceramics Using Laser Engineered Net Shaping. *Int. J. Appl. Ceram. Technol.* **2008**, *5* (3), 234-242.

166. Li, Y.; Hu, Y.; Cong, W.; Zhi, L.; Guo, Z., Additive manufacturing of alumina using laser engineered net shaping: Effects of deposition variables. *Ceram. Int.* **2017**, *43* (10), 7768-7775.
167. Niu, F.; Wu, D.; Ma, G.; Wang, J.; Guo, M.; Zhang, B., Nanosized microstructure of Al<sub>2</sub>O<sub>3</sub>-ZrO<sub>2</sub> (Y<sub>2</sub>O<sub>3</sub>) eutectics fabricated by laser engineered net shaping. *Scr. Mater.* **2015**, *95*, 39-41.
168. Will, J.; Melcher, R.; Treul, C.; Travitzky, N.; Kneser, U.; Polykandriotis, E.; Horch, R.; Greil, P., Porous ceramic bone scaffolds for vascularized bone tissue regeneration. *J. Mater. Sci.: Mater. Med.* **2008**, *19* (8), 2781-90.
169. Butscher, A.; Bohner, M.; Doebelin, N.; Hofmann, S.; Muller, R., New depowdering-friendly designs for three-dimensional printing of calcium phosphate bone substitutes. *Acta Biomater.* **2013**, *9* (11), 9149-9158.
170. Crump, S. S. Apparatus and method for creating three-dimensional objects. US5121329A, June 9, 1992.
171. Yardimci, A. M.; Guceri, S. I.; Danforth, S. C.; Agarwala, M.; Safari, A. In *Numerical modeling of fused deposition processing*, ASME International Mechanical Congress and Exposition, San Francisco, CA, Rutgers, The State University of New Jersey: San Francisco, CA, 1995.
172. Mohamed, O. A.; Masood, S. H.; Bhowmik, J. L., Optimization of fused deposition modeling process parameters for dimensional accuracy using I-optimality criterion. *Meas.* **2016**, *81*, 174-196.
173. Chohan, J. S.; Singh, R.; Boparai, K. S.; Penna, R.; Fraternali, F., Dimensional accuracy analysis of coupled fused deposition modeling and vapour smoothing operations for biomedical applications. *Composites, Part B* **2017**, *117*, 138-149.
174. Griffin, C. W.; Daufenbach, J.; McMillan, S. In *Solid Freeform Fabrication of Functional Ceramic Components Using a Laminated Object Manufacturing Technique*, 1994 International Solid Freeform Fabrication Symposium, Austin, TX, The University of Texas at Austin: Austin, TX, 1994.
175. Kim, G. D.; Oh, Y. T., A benchmark study on rapid prototyping processes and machines: Quantitative comparisons of mechanical properties, accuracy, roughness, speed, and material cost. *Proc. Inst. Mech. Eng., Part B* **2008**, *222* (2), 201-215.
176. Khajavi, S. H.; Partanen, J.; Holmström, J., Additive manufacturing in the spare parts supply chain. *Comput. Ind.* **2014**, *65* (1), 50-63.

177. Wen, Y.; Xun, S.; Haoye, M.; Baichuan, S.; Peng, C.; Xuejian, L.; Kaihong, Z.; Xuan, Y.; Jiang, P.; Shibi, L., 3D printed porous ceramic scaffolds for bone tissue engineering: a review. *Biomater. Sci.* **2017**, *5* (9), 1690-1698.
178. Hollister, S. J., Porous scaffold design for tissue engineering. *Nat. Mater.* **2005**, *4* (7), 518-24.
179. James, W. J.; Slabbekoorn, M. A.; Edgin, W. A.; Hardin, C. K., Correction of congenital malar hypoplasia using stereolithography for presurgical planning. *J. Oral Maxillofac. Surg.* **1998**, *56* (4), 512-517.
180. Jardini, A. L.; Larosa, M. A.; Filho, R. M.; Zavaglia, C. A. d. C.; Bernardes, L. F.; Lambert, C. S.; Calderoni, D. R.; Kharmandayan, P., Cranial reconstruction: 3D biomodel and custom-built implant created using additive manufacturing. *J. Cranio. Maxill. Surg.* **2014**, *42* (8), 1877-1884.
181. Withell, A.; Diegel, O.; Grupp, I.; Reay, S.; de Beer, D.; Potgieter, J., Porous ceramic filters through 3D printing. In *Innovative Development in Virtual and Physical Prototyping*, 1st ed.; Bártolo, P. J., Ed. CRC Press: Leiden, The Netherlands, 2011; pp 313-318.
182. Fielding, G. A.; Bandyopadhyay, A.; Bose, S., Effects of silica and zinc oxide doping on mechanical and biological properties of 3D printed tricalcium phosphate tissue engineering scaffolds. *Dent. Mater.* **2012**, *28* (2), 113-22.
183. Makovec, R. In *Digital Technologies in Dental Laboratories*, 21st International DAAAM Symposium Vienna, Austria, Katalinic, B., Ed. DAAAM International: Vienna, Austria, 2010.
184. Suwanprateeb, J.; Sanngam, R.; Suvannapruk, W.; Panyathanmaporn, T., Mechanical and in vitro performance of apatite-wollastonite glass ceramic reinforced hydroxyapatite composite fabricated by 3D-printing. *J. Mater. Sci.: Mater. Med.* **2009**, *20* (6), 1281-1289.
185. Di Prima, M.; Coburn, J.; Hwang, D.; Kelly, J.; Khairuzzaman, A.; Ricles, L., Additively manufactured medical products – the FDA perspective. *J. 3D Print. Med.* **2016**, *2* (1), 1.
186. Morrison, R. J.; Kashlan, K. N.; Flanagan, C. L.; Wright, J. K.; Green, G. E.; Hollister, S. J.; Weatherwax, K. J., Regulatory Considerations in the Design and Manufacturing of Implantable 3D-Printed Medical Devices. *Clin. Transl. Sci.* **2015**, *8* (5), 594-600.
187. Zadpoor, A. A.; Malda, J., Additive Manufacturing of Biomaterials, Tissues, and Organs. *Ann. Biomed. Eng.* **2017**, *45* (1), 1-11.

188. Pappas, J. M.; Dong, X., Porosity characterization of additively manufactured transparent MgAl<sub>2</sub>O<sub>4</sub> spinel by laser direct deposition. *Ceramics International* **2020**, *46* (5), 6745-6755.
189. Yao, Q.; Zhang, L.; Jiang, Z.; Huang, G.; Zhou, T.; Ben, Y.; Wei, S.; Sun, R.; Chen, H.; Wang, Y., Isobam assisted slurry optimization and gelcasting of transparent YAG ceramics. *Ceram. Int.* **2018**, *44* (2), 1699-1704.
190. Lu, Y.; Gan, K.; Huo, W.; Lv, L.; Liu, J.; Zhang, X.; Yan, S.; Yang, J., Dispersion and gelation behavior of alumina suspensions with Isobam. *Ceram. Int.* **2018**, *44* (10), 11357-11363.
191. Sun, Y.; Shimai, S.; Peng, X.; Zhou, G.; Kamiya, H.; Wang, S., Fabrication of transparent Y<sub>2</sub>O<sub>3</sub> ceramics via aqueous gelcasting. *Ceram. Int.* **2014**, *40* (6), 8841-8845.
192. Yang, Y.; Wu, Y., Tape-casted transparent alumina ceramic wafers. *J. Mater. Res.* **2014**, *29* (19), 2312-2317.
193. Yang, Y.; Wu, Y., Environmentally benign processing of YAG transparent wafers. *Opt. Mater. (Amsterdam, Neth.)* **2015**, *50* (Part A), 32-35.
194. Yang, Y.; Liu, Y.; Shimai, S.; Wu, Y., Environmentally Friendly Processing of Transparent Optical Ceramics. In *Green and Sustainable Manufacturing of Advanced Material*, 1st ed.; Singh, M.; Ohji, T.; Asthana, R., Eds. Elsevier: Oxford, 2016; pp 497-548.
195. Mamatha, S.; Biswas, P.; Ramavath, P.; Das, D.; Johnson, R., 3D printing of complex shaped alumina parts. *Ceram. Int.* **2018**, *44* (16), 19278-19281.
196. Rueschhoff, L.; Costakis, W.; Michie, M.; Youngblood, J.; Trice, R., Additive Manufacturing of Dense Ceramic Parts via Direct Ink Writing of Aqueous Alumina Suspensions. *Int. J. Appl. Ceram. Technol.* **2016**, *13* (5), 821-830.
197. Wilson, S. A.; Cross, L. M.; Peak, C. W.; Gaharwar, A. K., Shear-Thinning and Thermo-Reversible Nanoengineered Inks for 3D Bioprinting. *ACS Appl. Mater. Interfaces* **2017**, *9* (50), 43449-43458.
198. Rezende, R. A.; Bártolo, P. J.; Mendes, A.; Filho, R. M., Rheological behavior of alginate solutions for biomanufacturing. *J. Appl. Polym. Sci.* **2009**, *113* (6), 3866-3871.
199. Wang, S. F.; Zhang, J.; Luo, D. W.; Gu, F.; Tang, D. Y.; Dong, Z. L.; Tan, G. E. B.; Que, W. X.; Zhang, T. S.; Li, S.; Kong, L. B., Transparent ceramics: Processing, materials and applications. *Prog. Solid State Chem.* **2013**, *41* (1), 20-54.

200. Seidel, J.; Claussen, N.; Rödel, J., Reliability of alumina ceramics: Effect of grain size. *J. Eur. Ceram. Soc.* **1995**, *15* (5), 395-404.
201. Chantikul, P.; Bennison, S. J.; Lawn, B. R., Role of Grain Size in the Strength and R-Curve Properties of Alumina. *J. Am. Ceram. Soc.* **1990**, *73* (8), 2419-2427.
202. Roy, R. S.; Guchhait, H.; Chanda, A.; Basu, D.; Mitra, M. K., Improved sliding wear-resistance of alumina with sub-micron grain size: A comparison with coarser grained material. *J. Eur. Ceram. Soc.* **2007**, *27* (16), 4737-4743.
203. Chen, I. W.; Wang, X. H., Sintering dense nanocrystalline ceramics without final-stage grain growth. *Nature* **2000**, *404* (6774), 168-71.
204. Wang, X.-H.; Chen, P.-L.; Chen, I.-W., Two-Step Sintering of Ceramics with Constant Grain-Size, I. Y<sub>2</sub>O<sub>3</sub>. *J. Am. Ceram. Soc.* **2006**, *89* (2), 431-437.
205. Wang, C.-J.; Huang, C.-Y.; Wu, Y.-C., Two-step sintering of fine alumina–zirconia ceramics. *Ceram. Int.* **2009**, *35* (4), 1467-1472.
206. Kim, B.-N.; Dash, A.; Kim, Y.-W.; Morita, K.; Yoshida, H.; Li, J.-G.; Sakka, Y., Low-temperature spark plasma sintering of alumina by using SiC molding set. *J. Ceram. Soc. Jpn.* **2016**, *124* (10), 1141-1145.
207. Yang, Q.; Zeng, Z.; Xu, J.; Zhang, H.; Ding, J., Effect of La<sub>2</sub>O<sub>3</sub> on Microstructure and Transmittance of Transparent Alumina Ceramics. *J. Rare Earths* **2006**, *24* (1), 72-75.

## VIII. APPENDIX

### 1. Table of Relative Density and Grain Size Data Among Sintered Samples.

Process	Sintering type	Temperature	Hold time	Average Relative Density (%)	Average Grain Size ( $\mu\text{m}$ )
3D Printed	SSS	1650	6	$98.24 \pm 0.32$	$7.36 \pm 1.21$
3D Printed	SSS	1750	6	$98.46 \pm 0.35$	$25.74 \pm 2.84$
3D Printed	SSS	1800	6	$99.06 \pm 0.36$	$45.25 \pm 7.23$
3D Printed	SSS	1850	2	$99.26 \pm 0.26$	$43.56 \pm 17.42$
3D Printed	SSS	1850	4	$99.45 \pm 0.19$	$57.89 \pm 9.77$
3D Printed	SSS	1850	6	$99.41 \pm 0.33$	$94.01 \pm 9.47$
3D Printed	SSS	1850	8	$99.36 \pm 0.34$	$108.11 \pm 17.36$
3D Printed	SSS	1850	10	$99.37 \pm 0.30$	$114.89 \pm 18.604$
3D Printed	SSS	1875	6	$99.91 \pm 0.08$	$113.27 \pm 17.48$
3D Printed	TSS	1850, 1800	8	$99.61 \pm 0.17$	$57.90 \pm 9.91$
3D Printed	TSS	1875, 1800	8	$99.92 \pm 0.03$	$87.69 \pm 13.53$
CIP	SSS	1850	2	$99.42 \pm 0.09$	n/a
CIP	SSS	1850	4	$99.72 \pm 0.17$	n/a
CIP	SSS	1850	6	$99.79 \pm 0.14$	n/a
CIP	SSS	1850	8	$99.74 \pm 0.14$	n/a
CIP	SSS	1850	10	$99.67 \pm 0.21$	n/a
CIP	TSS	1850, 1800	8	$99.89 \pm 0.08$	n/a
CIP	TSS	1875, 1800	8	$99.93 \pm 0.05$	n/a